SSRG International Journal of Mechanical Engineering
ISSN: 2348-8360/ https://doi.org/10.14445/23488360/IJME-V13I5P105

Volume 13 Issue 5, 56-82, May 2026

Original Article

Experimental Investigation and Data Driven Prediction of Al6061-SiC-Gr Hybrid Composites

Chattenahally Ramegowda Vishwanath[1], Raviraj Mahadevappa Sunkapur[2], Rathan Kumar Krishna Murthy[3]

[1,2]*Government Engineering College, Chamarajanagar, Karnataka, India.*
[1,2]*Visvesvaraya Technological University, Belagavi, Karnataka, India.*
[3]*Government Engineering College, Kushalnagar, Karnataka, India.*

[1]*Corresponding Author : crvishwanathgttc@gmail.com*

Received: 10 February 2026 Revised: 20 March 2026 Accepted: 20 April 2026 Published: 29 May 2026

Abstract *- Al6061-based metal matrix composites are mostly used in structural and tribological properties due to their exceptional mechanical performance and lightweight nature. Reliable data-driven models are necessary since it is difficult to forecast composite characteristics accurately due to variations in processing circumstances as well as reinforcing content. The experimental examination and data-driven prediction of stir-cast Al6061-SiC-Gr hybrid composites are the main objectives of this work. To assess their mechanical, tribological, and physical characteristics, composites containing different weight percentages of graphite and silicon carbide were created. Standard protocols were followed in the experimental measurement of density, porosity, hardness, tensile strength, elongation, and wear properties. The impact of unreinforced, single-reinforced, and hybrid composite material performance was thoroughly investigated. To forecast properties, a Depth Adaptive Deep Neural Network (DADNN) was created and combined with an Improved Chicken Swarm Optimization Algorithm (iCSOA). Statistical performance indicators were used to train, validate, and test the proposed model using experimental data. Results indicated that the proposed model provides high prediction accuracy with 0.012 MAE, 0.015 RMSE, 0.0009 MSE, 0.998* R^2*, 0.143 MAPE, and 0.011 SDE and outperforms conventional approaches in estimating the properties of composite materials.*

Keywords *- Silicon carbide, Two-stage stir casting, Microstructural Characterization, Normalization, and Deep Learning.*

1. Introduction

Metal Matrix Composites (MMCs) made from alloys of aluminum, especially Al6061, have gained major interest in various industries because of their beneficial balance of mechanical, corrosion-resistant, and thermal characteristics. These composites are becoming popular in the mechanical sector, where minimization of weight and maintenance of strength are important [1]. Aluminium is ranked the 2nd most used material in industry after steel, and this indicates its significant contribution in the manufacturing industry today [2]. A major characteristic of aluminium is that it is resistant to corrosion by nature [3]. When exposed to air, aluminum quickly creates a thin but protective oxide film (Al2O3), which acts as a layer of passivation to prevent additional oxidation of the base metal. Steel, on the other hand, tends to flake and corrode under similar conditions. Aluminium also displays better resilience in humid as well as salty conditions, thereby making it beneficial for marine applications [4]. In spite of the advantages, the cost of making MMCs is usually higher compared to that of conventional monolithic metals. However, methods of mass production have shown the ability to decrease costs, which makes MMCs an affordable choice for applications that require exceptional performance when economies of scale are taken into account. Among the various MMC fabrication techniques available, the synthesis approach significantly affects the final cost as well as the performance of the composite [5].

Powder Metallurgy (P/M) is a technology that is used to compact the powdered metals and sinter them at high temperatures. It is one often used technique for fabrication [6]. This approach delivers refined and highly uniform microstructures, but the entire procedure is relatively costly because of the powder production cost and energy-consuming sintering process. A different approach, Chemical Vapor Deposition (CVD), gives superior control throughout the deposition of materials at the level of molecules but is restricted by high operational cost and complexity [7]. On the other hand, stir casting has become an economical as well as practical liquid-state processing technique for creating composites based on aluminium [8, 9]. It enables a homogeneous incorporation of the reinforcements into the melting matrix, in particular, when the appropriate mixing parameters and additive preliminary treatments are employed [10]. Stir casting has become a favored process because of its applicability and simplicity in large-scale use in the research of industrial and academic MMC [11]. Other methods of fabrication, such as Spark Plasma Sintering (SPS) and recent molding procedures, are also explored because of their ability to produce composites of thick and high-performance, especially in situations where complex shapes or special microstructures are required [12]. These techniques have proven to be effective but also tend to be trade-offs in the form of cost or process control [13]. Manufacturing systems have become more intelligent, flexible, and dependent on data in recent years [14]. The use of Artificial Intelligence (AI) approaches in the area of materials research has received a lot of interest [15]. As materials science keeps on developing, the availability of a variety of sources that contain large amounts of experimental as well as computational data can be utilized to different approaches driven by data, including Deep Learning (DL) for solving challenging issues. One region of focus is the use of predictive modeling in relation to MMC, an alloy group alongside a variety of applications in industry because of its beneficial characteristics.

Several existing studies have been reviewed in order to assess the performance characteristics. Bharath et al. [16] examined Al6061/SiC/graphite hybrid composites made by stir casting and assessed their yield strength as well as hardness for different amounts of reinforcement. The composite containing 6 weight percent SiC and 7 weight percent graphite showed the maximum hardness of about 11.23 and yield strength of about 214.85 N/mm², with increases of 55.11% and 25.09% over the basic alloy. The findings from the experiment were validated using a predictive model developed using Linear Regression (LR), which achieved a prediction accuracy was 93.18% throughout training as well as 73.59% throughout testing. Further, fracture behavior as well as effective interfacial bonding were validated by SEM analysis. However, the capacity to extract nonlinear interactions along with hybrid MMC networks is limited by the application of LR. Rajput et al. [17] investigated the use of ML methods to forecast the mechanical characteristics of stir-cast hybrid metal matrix composites, which are made of aluminum. It also examined how material and process characteristics affected composite performance using Al7075 along with Al6061 as basis matrices. Several ML models were trained as well as tested using experimental mechanical property data, with the Decision Tree (DT) regression technique achieving the greatest prediction accuracy of about 92.03% over ultimate tensile strength. The predicted tensile strength results agreed well with the experimental findings, with errors of fewer than 10%. Although the technique was restricted to traditional ML approaches along with a single mechanical feature, it showed how ML effectively reduced experimental expense and labor.

Nithya et al. [18] used ML and optimization tools to examine the effects of reinforcement composition and stir casting process variables on the mechanical characteristics of TiO_2-reinforced aluminum alloy composites. In order to maximize hardness, tensile strength, and impact strength, it also used the Taguchi technique to find the ideal melt temperature, stirring speed, and reinforcing weight percentage. The ideal parameters were found to be 600 °C processing temperature, 9 weight percent reinforcing content, and 600 rpm stirring speed. The ML model showed outstanding predictive performance with an R^2 value of about 99.5%, which shows a high degree of agreement between the predicted and experimental outcomes. Golla et al. [19] used an integrated experimental as well as ML method to examine the mechanical performance and wear behavior of aluminum matrix hybrid nanocomposites reinforced with titanium carbide with variable graphite content. Ultrasonic-assisted stir casting was used to create the composites, and microstructural analysis verified consistent reinforcement dispersion along with grain refinement. The Al-4 weight percent graphite composite had the best mechanical performance, with notable increases in yield strength, tensile strength, and hardness. Due to the creation of a lubricating tribo-layer, tribological analysis showed significant decreases in wear rate as well as coefficient of friction with increasing graphite content. Numerous wear processes were found, which include adhesion, oxidation, delamination, plastic deformation, and abrasion. When predicting wear rate, a Random Forest (RF) regression technique demonstrated great predictive accuracy, with an R^2 value of 0.93.

Sarat Babu et al. [20] investigated the dry sliding wear behavior of Al7075 metal matrix composites reinforced with carbon nanotubes utilizing a pin-on-disc configuration. Reinforcement content, normal load, sliding velocity, and sliding distance effects on the wear rate and coefficient of friction were analyzed in an organized manner using 108 experimental trials. SEM of the worn specimen showed that the major wear processes mainly involved abrasion, adhesion, oxidation, and delamination. In order to model and predict tribological performance, multiple ML algorithms, including polynomial regression, multilayer perceptron, RF, and Support Vector Regression (SVR), were developed and compared. The SVR model showed the best prediction accuracy of wear rate with an R^2 of 98.76, whereas the RF model had high predictive accuracy of the coefficient of friction with an R^2 of 98.71. Kolev et al. [21] created a hybrid deep learning and ensemble learning model (DL-EL) that uses Multi-Layer Perceptron and Gradient Boosting to predict Cu-Ni-Si alloy characteristics. Additionally, GridSearchCV and Genetic Algorithms were used to tune the hyperparameters of the DL-EL model. The results showed that the DL-EL model was passing the test with an R^2 value of 0.98. Additionally, a feature significance analysis showed that copper has a significant impact on the mechanical characteristics of Cu-Ni-Si alloys.

The mechanical properties of Graphene-Reinforced Aluminum Matrix Composites (GAMCs) were predicted by Kumar et al. [22] using a Sequential Average Generative

Discrimination Neural Network (SAGDNN). In order to maximize speed and convergence, the crested porcupine optimizer was employed. Additionally, model predictions were analyzed using explainable AI techniques like GC-SHAP, which revealed that the most important factors influencing hardness were aluminum and the ball-to-powder weight ratio. The results of the research demonstrated that the SAGDNN model performed well, having an MAPE for hardness and tensile strength $< 2\%$. Mishra and Baradeswaran [23] integrated an experimental as well as data-driven approach to study the tribological performance of AA7075, and it was reinforced with in-situ formed Al_3Ti and TiB_2 particulates. In order to forecast wear rate and friction coefficient, as well as to complement the RSM Response Surface Methodology (RSM), it was compared with ML models such as Deep Neural Network (DNN), SVR, Extreme Gradient Boosting (XGB), and RF. Furthermore, the effects of the key standard processing parameters were quantified using explainable AI (SHAP), with temperature and applied load identified as the most critical parameters. The results have demonstrated a reduction in experimental efforts and an improvement in prediction accuracy. On the other hand, the study is limited to specific tribological characteristics and is based on conventional ML techniques. Hybrid Deep Neural Network-based Salp Swarm Optimization (DNN-SSO) was created by Saminathan and Lakshmipathy [24] to forecast and validate the mechanical characteristics of Al7050 and Al7075 composites that were acquired through experimentation. It was then compared with existing neural network-based models. The results showed that the suggested model accurately predicted the mechanical characteristics and correlated best with experimental data.

Despite extensive studies on Al6061-based hybrid metal matrix composites, a number of issues still exist. Most existing studies are largely reliant on experimental trial and error techniques that are costly, time-consuming, and limited to certain composition ranges. Moreover, traditional machine learning models have been frequently used, but these models cannot represent the complex nonlinear interactions between different reinforcing materials. Furthermore, most previous studies concentrate on forecasting particular characteristics, such as mechanical or tribological behavior, independently. Also, very little research has been done using hybrid DL models. Also, these models have been used to predict properties of composites, but often a fixed network design is used; there are no adaptive depth mechanisms to capture the varying complexity of features. Moreover, implementing deep learning models with advanced optimization methods to enhance the accuracy of predictions has been less explored. Furthermore, a lot of existing research uses limited or less varied datasets, which has an impact on the created models' resilience and capacity to generalize across different material compositions and process circumstances. Thus, there is a requirement for a combined experimental and advanced data-driven algorithm that can simultaneously model various properties and accurately predict the nonlinear behavior of hybrid composites. This study seeks to solve such an issue by coming up with a hybrid predictive model based on deep learning and optimization.

The motivation behind the current research is the necessity to create an elaborate experimental and data-based framework that can successfully predict the physical, mechanical, and tribological characteristics of Al6061-SiC-graphite composites correctly. The study is expected to minimize the dependency of experiments by combining systematic experimentation with deep learning and optimization methods, extend the predictive reliability, and contribute to the efficient design of high-performance hybrid composites. The main objectives of this study are:

- To fabricate Al6061-SiC, Al6061-graphite, and Al6061-SiC-graphite hybrid composites using stir casting.
- To evaluate the physical, mechanical, and tribological properties of the fabricated composites.
- To investigate the effect of individual and hybrid reinforcement on composite performance.
- To create a deep learning-based prediction model for predicting composite properties.
- To identify the best-performing composite composition based on strength and wear resistance.

This study presents a novel, consolidated experimental and data-driven approach for Al6061-SiC-Gr hybrid composites that addresses key shortcomings of the existing literature. The study employs a Depth Adaptive Deep Neural Network (DADNN) that is capable of effectively capturing complex nonlinear interactions between large numbers of different reinforcement materials, in contrast to traditional methods, which are based on classical ML models. The proposed DADNN-iCSOA model, which includes an adaptive depth neural network model that flexibly changes its depth and structure of the network to learn complex nonlinear relationships efficiently, is not addressed in existing models. Moreover, a multi-output prediction model is introduced that simultaneously predicts mechanical, tribological, and physical properties. Also, using the Improved Chicken Swarm Optimization Algorithm (iCSOA) improves prediction performance by maximizing the accuracy of model parameters and by avoiding local minima. Also, the data augmentation strategy based on ADASYN is employed to enhance the data diversity and the ability of the model to generalize when overcoming the limitation of a small experimental dataset. To ensure uniformity and reliability, there is also a prediction on the basis of experimental results and experimental confirmation.

The paper is organized as follows: Section 2 provides the details about the materials, mix proportion, fabrication process, experimental test, microstructural characterization, and prediction model. Section 3 includes the results and discussion of the experimental assessment and the prediction model. Finally, section 4 concludes the study and future scope of the study.

2. Materials and Methodology

The current research paper is aimed at designing and analysing Al6061 composite reinforcement with SiC and Gr particles. Initially, the materials were fabricated using a two-stage stir casting technique in order to achieve improved particle distribution as well as better interfacial bonding. Standard testing procedures were used to test the fabricated composites on physical, mechanical, and tribological properties. Microstructural experiments have been performed to determine the relationship between reinforcement arrangement and the composite performance.

The data gathered through the experiment was then applied to the prediction and optimization of the behavior of hybrid composite materials. The experimental dataset was preprocessed using IQR, min-max normalization, and ADASYN data augmentation for consistency and completeness before being used for prediction modeling. Then, the preprocessed dataset was split into 70% samples for training, 15% for samples for validation, and 15% for samples for testing.

Then, a proposed iCSOA optimized DADNN model was employed to predict the nonlinear relationship between reinforcement composition and composite properties. The performance was evaluated using various performance metrics to assess the efficacy of the proposed model. To ensure consistency in prediction evaluation, numerous approaches, including Decision Tree (DT), Linear Regression (LR), Multi-layer Perceptron (MLP), Random Forest (RF), and Support Vector Regression (SVR), were used for comparison under the same experimental setup as the proposed method. Figure 1 represents the workflow of this present study.

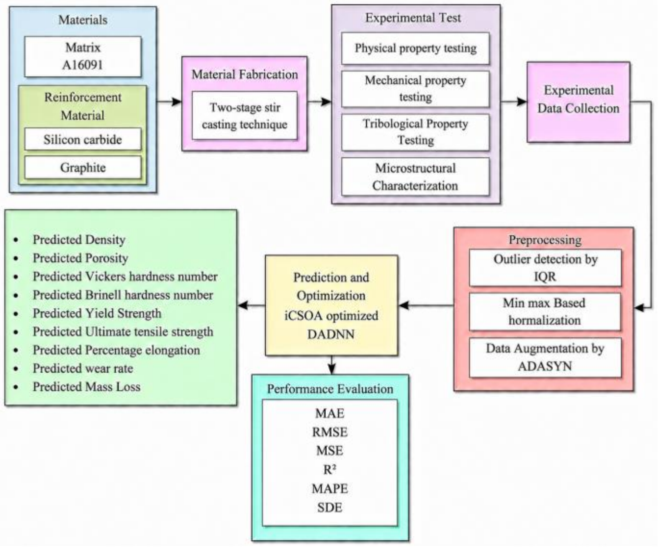

Fig. 1 Proposed Methodology

2.1. Matrix Material

Due to the qualities like toughness, good corrosion resistance, and moderate strength in comparison to other aluminium alloys, Al6061 is selected as the matrix material for preparing the hybrid metal matrix composite in this work. This material finds extensive use in the automotive, marine, and construction industries. The chemical composition of the Al6061 is shown in Table 1, and the Al-6061 ingot was procured from a commercial aluminium smelting company.

Table 1. Chemical Composition of Al6061 [25]

Element	Composition
Al	Balance
Mg	0.8-1.2
Zn	0.15-0.40
Si	0.6-1.0
Mn	0.2-0.8
Ti	0.1
Fe	0.5
Cr	0.1

2.2. Reinforcement Materials

This work uses ceramic and solid lubricant particles, namely, SiC and Gr materials, as reinforcement materials to make the hybrid composite material.

2.2.1. Silicon Carbide (SiC)

SiC is a useful reinforcing material for improving the mechanical performance of composites composed of aluminum because it is substantially tougher than aluminum. Figure 2 shows the visual representation of the SiC. It contributes to homogeneous particle distribution without significant segregation throughout casting due to the density it has (3.21 g/cm³), which is quite near to that of aluminum. SiC excels many different reinforcing materials with regard to strength, corrosion resistance, and thermal conductivity. Additionally, it offers exceptional resistance to chemical assault as well as degradation, especially in decreasing conditions. Because of these characteristics, adding SiC to aluminum alloys increases their tensile and flexural strengths. Table 2 represents the physical properties of SiC.

Fig. 2 SiC Powder Used in this Study

Table 2. Physical Properties of SiC [26]

Properties	values
Morphology	Angular
Melting Point (ºC) 447	2730
Density (g/cm^3)	3.21

2.2.2. Graphite (Gr)

Due to exceptional self-lubricating properties and a low coefficient of friction, graphite was chosen as a reinforcement material in this study, which greatly improves the tribological performance of the composite. The addition of graphite contributes to it by reducing wear and surface damage, as SiC increases the hardness of the material at the expense of increased friction potential. This hexagonal structure of the graphite allows it to be used in contact surfaces and bearings, and thus it improves the lubricating behaviour of composites [27]. Also, graphite has good thermal conductivity, resulting in high heat elimination. Thus, the use of graphite guarantees a balanced enhancement of the hybrid composite's lubricating function, wear resistance, and mechanical strength.

2.3. Mix Proportions and Composition Details

The composition details of the unreinforced, singly reinforced, and hybrid composites used in this study are given in Table 3. In order to evaluate the individual and combined effects of SiC and Gr reinforcements in Al6061 matrix, the composition proportions were carefully selected. In this study, the SiC concentration was adopted from 5 wt. % to 15 wt. % in order to investigate the effect it had on wear resistance as well as strength. The quantity of the Gr was then adopted in this study between 1 wt. % and 5 wt. % to study the effect of the additive on lubrication and the reduction of friction. Hybrid compositions have been further developed to obtain the best trade-off between physical, mechanical, tribological, and microstructural behavior.

Table 3. Mix design of Al6061-SiC-graphite composites

Sample ID	Al6061 (wt.%)	SiC (wt.%)	Graphite (wt.%)	Composite type
S0	100	0	0	Base alloy
S1	95	5	0	Al-SiC
S2	90	10	0	Al-SiC
S3	85	15	0	Al-SiC
S4	99	0	1	Al-Gr
S5	97	0	3	Al-Gr
S6	95	0	5	Al-Gr
S7	94	5	1	Hybrid
S8	92	5	3	Hybrid
S9	90	5	5	Hybrid
S10	89	10	1	Hybrid
S11	87	10	3	Hybrid
S12	85	10	5	Hybrid
S13	84	15	1	Hybrid
S14	82	15	3	Hybrid
S15	80	15	5	Hybrid

2.4. Composite Fabrication Process

Composites were fabricated by the two-stage stir casting method. The two-step casting involves the placement of the aluminum ingot in a graphite crucible and heating it to 700°C until it melts, and then allowing it to cool until reaching the slurry stage. The particles of the reinforcing SiC and graphite were then preheated separately to remove moisture and decrease temperature gradients to facilitate simple mixing with the molten alloy. The reinforcing materials are then added to the slurry and mixed manually after heating. To make sure the particles were properly mixed, the mixture was warmed and stirred for 15 minutes at 500 rpm. After that, the liquid was put into a heated mold and allowed to cool to room temperature. For 30 minutes, the mold was warmed to 300 °C. Additionally, the materials were homogenized in a muffle furnace. The samples were heated and soaked in the furnace. The samples were then left to cool within the furnace for a further 24 hours after the furnace was shut off. Any internal tension that could have developed during the casting process was reduced by this approach. The sample was then machined and formed into a specimen for each test in accordance with ASTM.

2.5. Experimental Testing of Composite Properties

The fabricated composites were tested on physical, mechanical, and tribological properties through standard tests.

2.5.1. Physical Property Testing

The Archimedes principle was used to determine the hybrid composite's density. In the process, a sample of each composite mixture was employed. Each sample's mass was first determined in air, and then it was weighed while immersed in distilled water. The density of the composite was then determined using Equation (1).

$$Density = \frac{Mass_a}{Mass_a - Mass_w} \quad (1)$$

Where the mass of the sample in water is denoted by$Mass_w$, and the mass of the sample in water is represented by$Mass_a$. Using this method, the densities of the base metal and hybrid composites were measured. Furthermore, the percentage of porosity was calculated by comparing the experimental and theoretical densities. It is mathematically expressed by using Equation (2).

$$\%Porosity = \left(\frac{Density_{theoretical} - Density_{experimental}}{Density_{theoretical}}\right) \quad (2)$$

2.5.2. Mechanical Property Testing

Hardness Test

This study's hardness was evaluated using Vickers and Brinell hardness tests. According to ASTM E-384, which specifies a suitable range of loads for testing with a diamond indenter, the Vickers Hardness value for each composition was determined [24].

The formed indentation is evaluated and changed to a hardness value. A thin rhombus-shaped diamond indenter was used in the Knoop test, whereas a diamond pyramid indenter with a square base as well as an included angle of 136° was utilized in the Vickers test.

Smooth emery paper was used to polish the test samples' surfaces before the test. The hardness value was computed by measuring the indent that developed on the surface. To get the average hardness value, each specimen was examined for hardness at different, distinct locations. The experimental setup of Vickers hardness is shown in Figure 3.

The Brinell Hardness Test is done using a ball indenter that is typically composed of steel or hardened steel. The diameter of the indenter is 10 mm. To get rid of any dirt, the specimen is cleaned initially with acetone. After it is mounted on the table, a lever is applied to the indenter until it barely touches the specimen. Loads were applied at different places after the lever was further moved until the smaller dial's indication pointed to 3.

The load is lifted after 30 seconds. After that, the specimen is removed and examined for the indentation under a microscope. Then the indentation diameter is measured. According to Equation (3), the Brinell Hardness Number (BHN) is calculated by dividing the applied load by the indentation surface area.

$$BHN = \frac{2Load}{\pi Dia\left(Dia - \sqrt{Dia^2 - Dia_i^2}\right)} \quad (3)$$

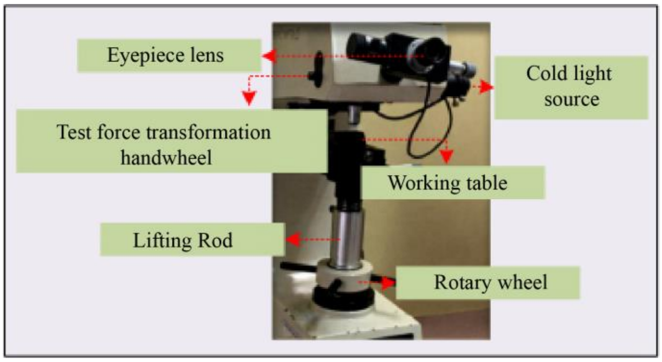

Fig. 3 Vickers Hardness Test Setup

Tensile Strength Test

An Instron universal testing machine, as shown in Figure 4, was used for tensile testing in order to assess the composites' tensile characteristics. As-cast composite cylindrical rods with a diameter of 15 mm and a length of 15 cm were machined into specimens for the test, which had a diameter of 5 mm and a gauge length of 30 mm. The specimens were placed on the testing apparatus and continuously pulled until fractured at a strain rate of 10-3/s. As advised by the ASTM 8M-91 standard, the tests were conducted at room temperature [25]. To ensure the accuracy of the data produced, three repeat tensile tests were conducted for every composite composition. The test evaluates the following tensile properties: yield strength, ultimate tensile strength, and percentage elongation.

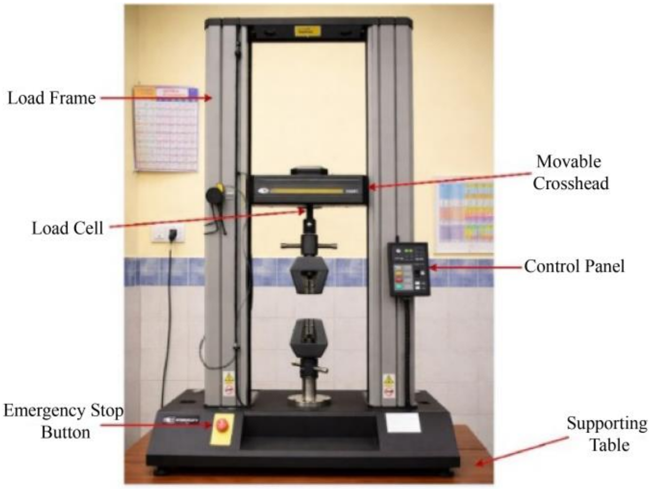

Fig. 4 Instron Universal Testing Machine

2.5.3. Tribological Property Testing

Two-Body Abrasive Wear Test

Figure 5 shows the test setup of the two-body abrasion wear test, where unreinforced and reinforced hybrid composite specimens were tested. According to ASTM G99, a pin-on-disc device was used to assess the produced composites' two-body abrasive wear performance [26]. To produce an abrasive interaction, the specimen was placed on a cylindrical pin that was 10 mm in diameter and 25 mm in height. It was then brought into contact with a revolving disc that was covered in SiC abrasive paper. The abraded SiC paper was taken out once the test was finished. A new SiC paper was adhered to the disk for every test. The specimen-containing pin was situated in the disc along a 20 mm Ø route. In order to evaluate wear behavior under various circumstances, the test was carried out by altering different loads and keeping a constant rotating speed. To investigate the wear resistance under repeated pass circumstances, various sliding distances were used. Acetone was used to clean the specimen's surface of dirt prior to and following the test, and it was thoroughly dried. A precise electronic scale was used to measure the beginning and final weights in order to calculate mass loss. The average of a number of trials was then reported.

Fig. 5 Two-Body Abrasive Wear Test setup

2.6. Microstructural Characterization

The microstructure of the unreinforced, singly reinforced, and hybrid composites was examined using Optical Microscopy, Scanning Electron Microscopy (SEM), Energy-Dispersive Spectroscopy (EDS), and X-ray Diffraction (XRD).

2.6.1. Optical Microscopy

The prepared sample was sectioned before being processed using typical metallographic procedures in an optical microscope inspection. After mounting, the samples were successively ground on different grades of emery paper to provide a smooth surface. Alumina slurry was then used for polishing in order to get a mirror-like finish. Once the specimens were polished, the surface was etched using the proper chemical reagent to reveal the microstructural characteristics as well as grain boundaries. After being etched, the samples were cleaned, dried, and examined at the proper magnifications using an optical microscope. This method was employed to study the grain structure, particle distribution, and overall microstructural uniformity of the composite.

2.6.2. Scanning Electron Microscopy (SEM)

High-resolution microstructural pictures of the produced samples were obtained by further examining them with a scanning electron microscope. Before the test, the polished samples were properly cleaned to get rid of any impurities. To increase the specimen's conductivity and prevent charging effects, a thin conductive coating was applied to its surface. The materials were examined in an SEM chamber. Following mechanical testing, SEM analysis provided precise information on the shape of fracture surfaces, porosity, and the dispersion of reinforcement interfacial bonding between the matrix and reinforcement.

2.6.3. Energy Dispersive Spectroscopy (EDS)

Energy dispersive spectroscopy (EDS) analysis was used for elemental mapping and dispersion analysis of the reinforcement particles in the matrix material. This was done using a field scanning electron microscope fitted with an EDS detector. The prepared sample was loaded into the SEM chamber, and then the testing region was directed by a focused electron beam. Through interaction between the sample and the electron beam, the constituent elements produced distinct X-rays. In order to identify the elements, these released X-rays have been identified and transformed into an energy spectrum. Finally, the elemental mapping was applied to investigate the distribution of the reinforcement particles, and quantitative data were generated in terms of weight percentage and atomic percentage. Elemental mapping was carried out to examine the distribution of reinforcement particles, and quantitative data were calculated via the calculation of weight % and atomic percentage.

2.6.4. X-Ray Diffraction (XRD)

The crystalline phases found in the produced composite were identified using X-ray diffraction analysis. Before testing, the surface of this product had been thoroughly cleaned and polished. The sample was then examined with monochromatic X-rays before it was placed into the XRD sample holder. According to Bragg's rule, diffraction patterns were generated as the X-rays interacted with the material's crystal surfaces. To determine the phases present, the diffracted intensity was measured throughout a chosen angular range, and the diffraction peaks that were acquired were compared with standard reference data. To validate the development of reinforcing phases and their structural stability in the matrix, the XRD analysis was conducted.

2.7. Experimental Data Collection

After completion of laboratory experimentation, the experimentally obtained data have been employed to predict the physical, mechanical, and tribological properties of Al6061-SiC-graphite composites. Also, these collected experimental results formed the primary input for developing and validating the proposed data-driven prediction model.

2.8. Data Preprocessing

The experimental data were verified to be complete and consistent before being used for modeling. The Interquartile Range (IQR) approach was used to identify any glaring outliers or inconsistent numbers in order to prevent excessive mistakes during model training. Equation (4) is used to calculate the interquartile range.

$$IQR = Quartile_3 - Quartile_1 \tag{4}$$

To measure all input and output variables within a comparable range, a minimum-maximum normalization was used, which normalizes all parameters. Equation (5) is the formula for min-max normalization.

$$N_{new} = \frac{N_{original} - Min_p}{Max_p - Max_p} \tag{5}$$

Where the given feature's maximum value is denoted byMax_p, the given feature's minimum value is represented byMin_p, the original value is denoted by$N_{original}$, and the new normalized value is represented byN_{new}. Additionally, using the ADASYN data augmentation technique, the models are improved by generating artificial samples from the data distribution. By concentrating more on challenging-to-learn examples, this method efficiently tackles class imbalance and enhances dataset variety. The more diverse the variety of input variables, the more the model will learn. Thus, reduces the risk of overfitting and enhances generalisation without the need to collect more experimental data.

2.9. Development of Prediction Model

To predict hybrid composites' properties, a hybrid iCSOA-optimized DADNN framework is developed in this study. As input variables, the proposed prediction model uses reinforcement composition characteristics such as graphite (wt.%), SiC (wt.%), and Al6061 (wt.%). Several output properties, including density, porosity, vickers hardness, Brinell hardness, yield strength, ultimate tensile strength, % elongation, wear rate, and mass loss, are predicted by this proposed hybrid prediction model based on these inputs. Initially, the Depth Adaptive Deep Neural Network architecture was used to forecast the nonlinear correlation between composite attributes and reinforcement composition. In order to determine the ideal DNN depth and provide fuzzy relevance weights to every DNN layer, Adaptive Neural Network Approaches are used. Additionally, this method was developed especially to train the deep neural network model and learn the network depth at the same time. The model hyperparameter and the relevance weight of each layer are formulated as a unique cost that maximizes the learning process. The network is composed of X layers. The X^{th}layer uses Equation (6) to apply a non-linear transformation $T$to the input P_j in order to generate the outputQ_j.

$$Q_j = T\left(P_j; N_p^T\right) \tag{6}$$

Where the set of network parameters (neuron weights) is represented byN_p, and the set of Minstance data that is provided as input to the deep learning algorithm is represented by$\left\{P_j\right\}_{j=1\ldots M}$. The network layers' iteratively fuzzy relevance weights are then learned by adding a layer relevance weight learning component. This is done by establishing the distance in layers$P$ between the input and mapped vectors. Equation (7) is used to calculate this distance using the Euclidean distance.

$$ED_{jk}^{X} = \left\| P_j^X - P_k^X \right\|_2 \tag{7}$$

Then, two methods, class-dependent ANNA and class-independent ANNA, are added to learn the fuzzy matching weights for each layer$X$. After every training block, class-dependent ANNA is introduced at iteration t to determine the fuzzy relevant weights of the layerWt_X^t. Using Equation (8), the class-independent objective function is created.

$$J = \sum_{i=1}^{R} \sum_{u=1}^{N^t} \sum_{j \in P^u} \sum_{k \epsilon P^u} \gamma_{ij} \gamma_{ik} \sum_{X=1}^{Num^t} Wt_X^t q \tag{8}$$

Where classes are represented by$R$, batches processed at$t$ by$N^t$and instances that are part of the batch processed at iteration$t$byP^u. Also, the number of layers at iteration t is represented byNum^t, the constant q regulates the degree of fuzziness of the learnt weights and $Wt_X^t$is the importance of the layer$X$at iteration$t$. This is followed by the addition of the class-dependent weights that learn the weights of the layers Wt_X^t, for each class$i$. Equation (9) is used to create the class-dependent objective function.

$$J = \sum_{i=1}^{R} \sum_{u=1}^{N^t} \sum_{j \in P^u} \sum_{k \epsilon P^u} \gamma_{ij} \gamma_{ik} \sum_{X=1}^{Num^t} Wt_X^t q - \lambda_i \left(\sum_{X=1}^{Num^t} Wt_{iX}^t - 1 \right) \tag{9}$$

Then Equation (10) is used to determine the layer fuzzy relevance weight by taking the maximum of the class fuzzy relevance weights.

$$Wt_X^t = Max_i\left(Wt_{iX}^t\right) \tag{10}$$

The layer pruning component begins to remove the irrelevant layers when the layer fuzzy relevance weights have finished learning. Because deepening the network will result in inadequate representation, the layer pruner method selects the layer with the highest weight and removes all subsequent layers. This suggests that deepening the network improves the representation. Then, the DADNN model hyperparameters, such as weight and bias, are successfully tuned by the iCSOA method.

To improve the global search capacity and prevent local minima during optimization, the Levy flying strategy and nonlinear decreasing inertia weight are added to the Improved Chicken Swarm Optimization method. The iCSOA approach integrates the Levy flight search strategy in the hen location update formula. Equation (11) represents the updated formula for the better hen's position.

$$Y_i^j(t+1) = Y_i^j(t) + S_1 * rand * \left(Y_{l1}^j(t) - Y_i^j(t)\right) + S_2 * rand * L_y(\lambda) \otimes \left(Y_{l2}^j(t) - Y_i^j(t)\right) \quad (11)$$

Where a scaling parameter in the interval [1, 3] is denoted by λ, a vector operator that represents point multiplication is represented by $\otimes$, and the jump route of a random search whose step size obeys the Levy distribution is represented by $L_y(\lambda)$. Furthermore, to update the chicks' location, nonlinear tactics of decreasing inertia weight are used. This enables the chicks to learn from themselves as well as from their mom. Equation (12) illustrates the nonlinear decreasing inertia weights updating ω.

$$W = W_{min_i}\left({W_{max_i}}/{W_{min_i}}\right)^{\left(1+ct/K\right)} \quad (12)$$

Where the maximal iterative number is represented by K, the minimum inertia weight is represented by min_i, and the maximum inertia weight is denoted by max_i. Overall, the proposed iCSO-based hybrid architecture dynamically removed unnecessary layers and adaptively adjusted DNN systems to increase prediction accuracy while reducing prediction error.

Figure 6 represents the architecture of the proposed model. Table 4 shows the hyperparameter details of the proposed model.

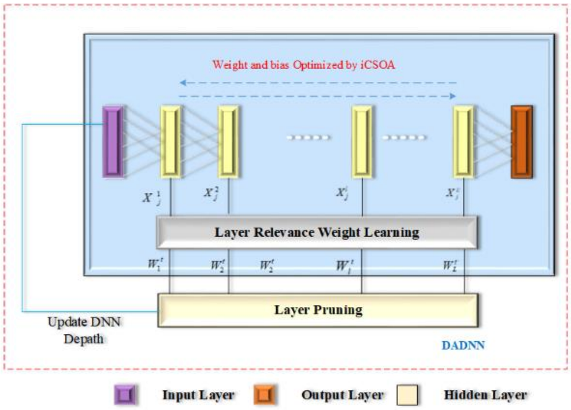

Fig. 6 Architecture of Proposed Model

Table 4. Hyperparameter details of the Proposed Model

Hyperparameters	Values
Activation function	ReLU
Kernel initializer	He Normal
Dropout rate	0.2
Learning rate	0.0001
Epochs	300
Batch size	32

2.10. Performance Evaluation

To analyze the accuracy of the proposed model in predicting composite materials properties, the following matrices were applied: Mean Absolute Error (MAE), Root Mean Square Error (RMSE), Mean Squared Error (MSE), Coefficient of Determination (R^2), Mean Absolute Percentage Error (MAPE), and Standard Deviation of Error (SDE). RMSE is a form of MSE that determines the square root of the mean squared error of the difference between the actual and the predicted value, whereas MSE determines the mean squared error between the predicted and the actual value. MAE gives the mean of the absolute differences between the anticipated and actual values. R^2 measures the fitness of the model. Equations (13) - (18) were used to calculate these statistical metrics.

$$MAE = \frac{1}{M}\sum_{j=1}^{M}\left|Q_j - \hat{Q}_j\right| \quad (13)$$

$$RMSE = \sqrt{\frac{1}{M}\sum_{j=1}^{M}\left(Q_j - \hat{Q}_j\right)^2} \quad (14)$$

$$MSE = \frac{1}{M}\sum_{j=1}^{M}\left(Q_j - \hat{Q}_j\right)^2 \quad (15)$$

$$R^2 = 1 - \frac{\sum_{j=1}^{M}\left(Q_j - \hat{Q}_j\right)^2}{\sum_{j=1}^{M}\left(Q_j - \bar{Q}_j\right)^2} \quad (16)$$

$$MAPE = \frac{1}{M}\sum_{j=1}^{M}\left|\frac{Q_j - \hat{Q}_j}{\hat{Q}_j}\right| \times 100 \quad (17)$$

$$SDE = \sqrt{\frac{1}{M-1} \times \sum_{j=1}^{M}\left[\left(Q_j - \hat{Q}_j\right) - ME\right]^2} \quad (18)$$

Where the number of observations is denoted by M, the j-th observation's actual value is represented by Q_j, the observation's forecast value is denoted by $\hat{Q}_j$, and the mean error is denoted by ME.

2.11. System Configuration Details

The system configuration details are labelled in Table 5.

Table 5. System Configuration

Parameters	Configuration
Processor	Intel(R) Core(TM) i7-4770 CPU @ 3.40 GHz
Installed RAM	16.0 GB (15.9 GB usable)
Graphics Card	Intel(R) HD Graphics 4600 (113 MB)
System type	64-bit operating system,x64-based processor
Python version	Python 3.10.14
Operating System	Windows 11 Pro, Version 24Hz

3. Result and Discussion

3.1. Experimental Outcomes

Figure 7 presents the result of the density obtained during the experimentation of 16 samples of hybrid Al6061-SiC- Gr composites. The original alloy of the sample S0 has a density of 2.70 gm/cm3, which is further refined by the incorporation of SiC in the Al6061. The maximum density of 2.83 g/cm^3 is obtained at the sample S3, under the composition of 85% Al6061 and 15% SiC.

Followed by this, the incorporation of Gr (1%, 3%, 5%) into the Al6061 significantly lowers the density to a value of 2.66 g/cm^3 at the sample S6. A significant rise in density is observed in the samples S7, S10, and S13 when the Al6061 and SiC (5%, 10%, 15%) are reinforced with 1% Gr. However, a steep decline is observed for the samples S8, S9, S11, S12, S14, and S15 when the Al6061 and SiC (5%, 10%, 15%) are reinforced with 3% and 5% Gr. The results indicate that the percentage content of the SiC and Gr is a major factors in determining the overall mass properties of the composite.

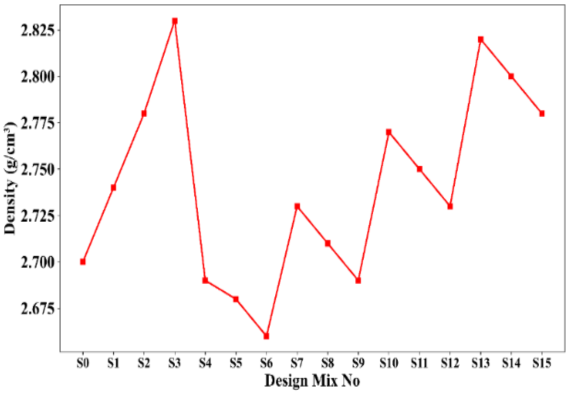

Fig. 7 Experimental Results of Density (g/cm^3)

The porosity results of the hybrid Al6061-SiC- Gr composite are illustrated in Figure 8. The Al6061 alloy in the sample S0 exhibited the lowest porosity with a value of 0.8% over all the other samples. Followed by this, the porosity gets increased at the sample S3 with a value of 2.9% for the composition of 85% Al6061 and 15% SiC.

The porosity value declines to 1.2% at the sample S4; however, it steadily rises until the sample S6, and this same pattern is observed until the sample S15. The maximum porosity is observed in the sample S15 with a value of 4.2% in the Al6061-SiC composite reinforced with 5% Gr.

The findings indicate that the maximum values result in an increase in the void space in the composite material, thereby lowering the material strength and its load-bearing capacity. The lower porosity offers enhanced mechanical strength, higher yield strength, and hardness in the composite material.

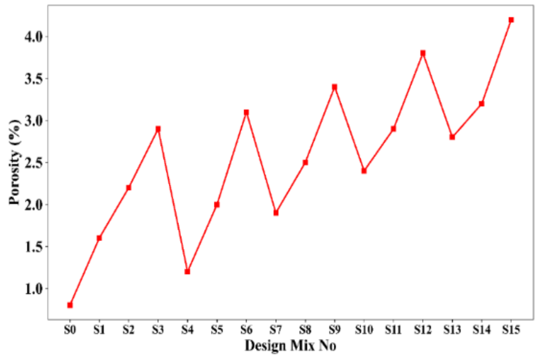

Fig. 8 Experimental Results of Porosity (%)

Figure 9 presents the experimental results of VHN retrieved through the 16 samples of the hybrid Al6061-SiC-Gr composite. The base alloy exhibited a VHN of 58 at the sample S0, which further rises steadily till sample S3. The sample S3 exhibited the highest VHN of 102 for the composition of 85% Al6061 and 15% SiC. Followed by this, the VHN steeply declined till the sample S6, which exhibits the lowest value of 52 for the composition of 95% Al6061 and 5% Gr. Followed by this, the VHN gets increased for the samples (S7, S10, S13) when the Al6061 and SiC are reinforced with 1% Gr, and the VHN gets lowered for the samples S8, S9, S11, S12, S14, and S15 when the Al6061 and SiC are reinforced with 3% and 5% Gr. The findings denote that the higher values of VHN enhance the hardness and wear resistance of the composite material.

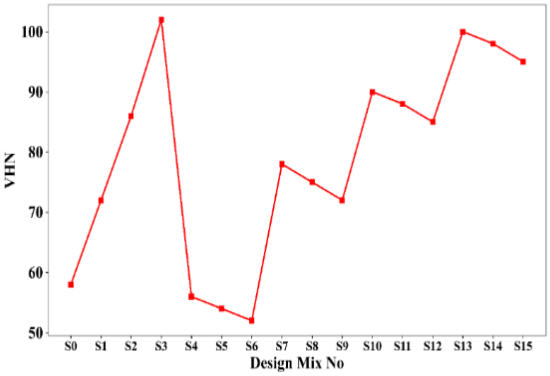

Fig. 9 Experimental Results of VHN

Figure 10 presents the experimental results of BHN attained by experimenting with 16 samples of the hybrid Al6061-SiC- Gr composite. The base alloy disclosed a BHN of 60 at the sample S0, which further rises steadily until sample S3. The sample S3 exhibited the highest BHN of 105 for the composition of 85% Al6061 and 15% SiC. After this, the BHN steeply declined till the sample S6, which reveals the lowest value of 54 for the composition of 95% Al6061 and 5% Gr. Followed by this, the BHN gets increased for the samples (S7, S10, S13) when the Al6061 and SiC are reinforced with 1% Gr, and the VHN gets lowered for the samples S8, S9, S11, S12, S14, and S15 when the Al6061 and SiC are reinforced with 3% and 5% Gr. The findings denote that the increasing rate of SiC to 15% significantly enhances the hardness of the composite material.

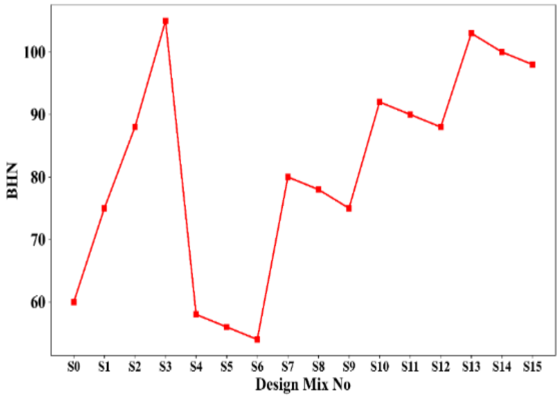

Fig. 10 Experimental Results of BHN

The experimental results of YS obtained by experimenting with 16 samples of a hybrid Al6061-SiC- Gr composite are given in Figure 11. The base material at sample S0 exhibits the YS of 95 MPa, which steeply rises toward the sample S3, exhibiting YS of 160 MPa, under the composition of 85% Al6061 and 15% Gr. After this, the YS gets decreased till the sample S6, which reveals the lowest value of 82 MPa, and then YS gets increased in the sample S7, and this trend is observed till the sample S15. The highest YS is observed in the sample S14 with a value of 165 MPa under the composition of 84% Al6061, 15% SiC, and 1% Gr. Overall, the findings convey that the higher values of YS increase the load-carrying capacity of the composite material without any structural damage.

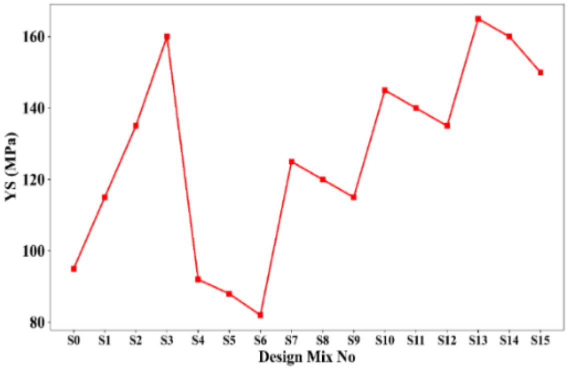

Fig. 11 Experimental Results of YS

Figure 12 illustrates the UTS experimental results of the 16 samples of hybrid Al6061-SiC- Gr composite. The base material exhibits a UTS of 130 MPa, which further rises steadily towards the sample S3, which exhibits a UTS of 205 MPa, under the composition of 85% Al6061 and 15% SiC. Further, the UTS steeply declined toward the sample S6, exhibiting a value of 112 MPa for the composition of 95% Al6061 and 5% Gr. Followed by this, UTS rises significantly towards the sample S7, and then reduces gradually till the sample S9, and this pattern can be observed till the sample S15. The maximum UTS is observed in the sample S14, which exhibits a value of 215 MPa for the composition of 82%Al6061, 15%SiC, and 3% Gr. In general, the findings demonstrate that the higher UTS significantly enhances the load-bearing capacity and can resist material damage against intense forces.

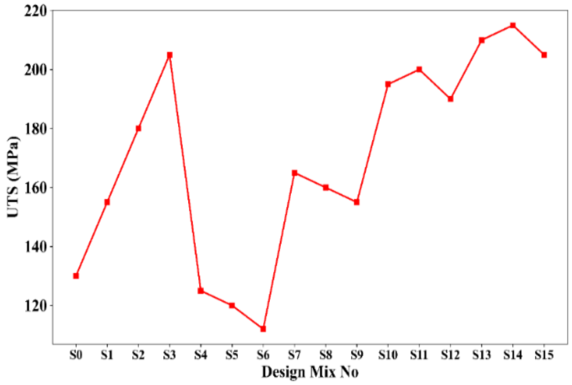

Fig. 12 Experimental Results of UTS

The experimental results for elongation across 16 samples of hybrid Al6061-SiC- Gr composite are illustrated in Figure 13. The experimental findings indicate that the trend is very fluctuating, where the elongation percentages are found to be at a minimum of 6.2 percent at sample S3 and at the maximum of 14 percent at sample S4. The base alloy, which is sample S0, has an elongation of 13.5%, which decreases further to sample S3. The sample S3 exhibits the lowest elongation of 6.2% for the composition of 85% Al6061 and 15% SiC. Followed by this, a steady rise is observed in sample S3 with a value of 14% under the composition of 99% Al6061 and 1% Gr. Further, the samples S5-S15 showed a fluctuating trend, with a small increase in the samples (S8, S9, S11, S12, S14, and S15), and a decreasing trend for the remaining samples. Overall, the findings reveal that the ductility of the material is significantly affected due to a reduction in elongation, which also facilitates the chance of brittleness in the material.

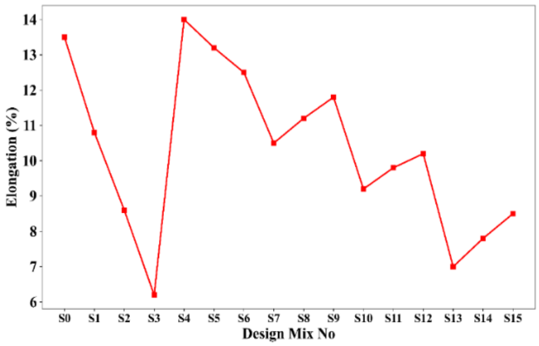

Fig. 13 Experimental Results of Elongation

The experimental results for wear rate over 16 samples of hybrid Al6061-SiC- Gr composite are given in Figure 14. The base material at sample S0 exhibits the highest wear rate of 4.8 mm^3/N-m among all the samples. Followed by this, a steep decline is observed till the sample S3, which is then followed by a steady increase towards the sample S4 with a value of 3.8 mm^3/N-m at a composition of 99% Al6061 and 1% Gr. The samples (S6-S15) exhibit a fluctuating pattern with small deviations. The sample S15 exhibits the lowest wear rate of 0.9 mm^3/N-m among all the samples. Altogether, the findings demonstrate that the lower value of wear rate enhances the material life, reduces maintenance costs, and increases durability.

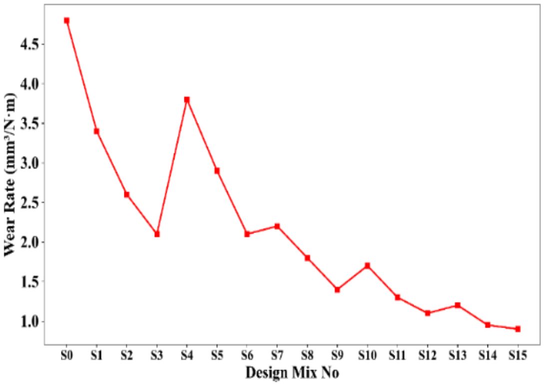

Fig. 14 Experimental Results of Wear Rate

The experimental results for mass loss over 16 samples of hybrid Al6061-SiC- Gr composite are given in Figure 15. The sample S0 exhibits the highest mass loss of 18.5 mg, which further declines to sample S3, exhibiting a value of 9.5 mg for the composition of 85% Al6061 and 15% SiC. The sample S4 rises steadily to a value of 13.9 mg for the composition of 99% Al6061 and 1% Gr. The samples from S6-S15 exhibit a similar pattern with a minimal deviation of the values. The least mass loss is noted in the sample S15, with the composition of 80% Al6061, 15% SiC, and 5% Gr, with a mass loss of 4.9 mg. In general, the results support the fact that the minimum mass loss enhances the surface integrity and structural strength of the composite material.

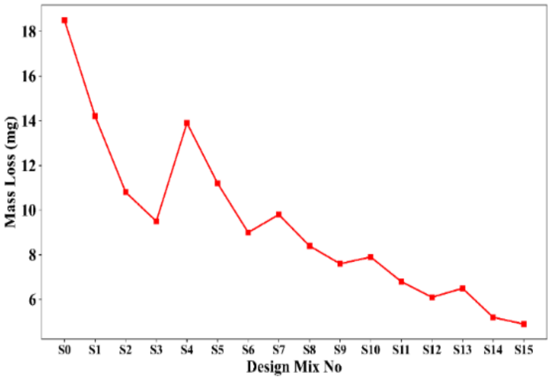

Fig. 15 Experimental Results of Mass Loss

3.2. Analysis of Physical Properties

The physical properties of the Al6061-SiC-Gr composite samples (S0-S15) in terms of density and porosity are presented in Table 6. The densities are between 2.66 and 2.83 g/cm³, and the porosities are in the range of 0.8%-4.2%. The baseline density of sample S0 is 2.7 g/cm³, and its porosity is 0.8%, which means the structure of this sample is relatively dense and defect-free. With a change of the reinforcement composition and processing conditions, an average increase in porosity is observed, with the samples S12 and S15 having porosity of 3.8% and 4.2%, respectively. In some instances, however, density is slightly lower (e.g., S6 with 2.66 g/cm³), indicating the presence of voids and poor particle distribution. Some samples, such as S3 and S13, have higher densities (2.83 g/cm³ and 2.82 g/cm³) even though they have moderate porosities, suggesting better packing of the particles and bonding. In general, the data show an inverse relationship between density and porosity for several samples, indicating the effect of dispersion of reinforcements and processing parameters on the integrity of the composite.

Table 6. Physical Properties of Al6061-SiC-Gr composite

ID	Density (g/cm³)	Porosity (%)
S0	2.7	0.8
S1	2.74	1.6
S2	2.78	2.2
S3	2.83	2.9
S4	2.69	1.2
S5	2.68	2
S6	2.66	3.1
S7	2.73	1.9
S8	2.71	2.5
S9	2.69	3.4
S10	2.77	2.4
S11	2.75	2.9
S12	2.73	3.8
S13	2.82	2.8
S14	2.8	3.2
S15	2.78	4.2

3.3. Analysis of Mechanical Properties

Table 7 presents the mechanical properties of the Al6061–SiC–Gr composite with different compositions (S0–S15), revealing the trend of hardness, strength, and ductility. The base sample S0 has relatively low hardness (58 VHN, 60 BHN), yield strength (95 MPa), and ultimate tensile strength (130 MPa) with good ductility of 13.5%. From S1 to S3, the reinforcement content has been increased, resulting in a considerable increase in hardness (up to 102 VHN, 105 BHN), strength (up to 160 MPa YS, 205 MPa UTS), and a corresponding decrease in elongation (from 12.8% to 6.2%), due to increased brittleness. Samples S4 to S6 show a contrasting trend as both hardness and strength decrease with an increase in elongation, indicating lesser reinforcement effectiveness. Samples S7-S12 exhibit moderate increases with a balance of strength and ductility. Samples S13 and S14 show the best performances in mechanical properties with hardness up to 100-103 VHN and strength reaching up to 165 MPa (YS) and 215 MPa (UTS), respectively, while the elongation remained relatively low (7-7.8%). The overall results suggest that the higher the reinforcement, the higher the hardness and strength, but the lower the ductility, which is the common relationship between strength and elongation in metal matrix composites.

Table 7. Mechanical Properties of Al6061-SiC-Gr composite

ID	VHN	BHN	YS (MPa)	UTS (MPa)	% Elongation
S0	58	60	95	130	13.5
S1	72	75	115	155	10.8
S2	86	88	135	180	8.6
S3	102	105	160	205	6.2
S4	56	58	92	125	14
S5	54	56	88	120	13.2
S6	52	54	82	112	12.5
S7	78	80	125	165	10.5
S8	75	78	120	160	11.2
S9	72	75	115	155	11.8
S10	90	92	145	195	9.2
S11	88	90	140	200	9.8
S12	85	88	135	190	10.2
S13	100	103	165	210	7
S14	98	100	160	215	7.8
S15	95	98	150	205	8.5

Table 8. Tribological Properties of Al6061-SiC-Gr composite

ID	Wear Rate ($mm^3/N{\cdot}m$)	Mass Loss (mg)
S0	4.8	18.5
S1	3.4	14.2
S2	2.6	10.8
S3	2.1	9.5
S4	3.8	13.9
S5	2.9	11.2
S6	2.1	9
S7	2.2	9.8
S8	1.8	8.4
S9	1.4	7.6
S10	1.7	7.9
S11	1.3	6.8
S12	1.1	6.1
S13	1.2	6.5
S14	0.95	5.2
S15	0.9	4.9

3.4. Analysis of Tribological Properties

The tribological properties of Al6061-SiC-Gr composites under different sample conditions (S0-S15) are shown in Table 8. From S0 to S15, it is clear that both wear rate and mass loss decrease progressively, reflecting an increasing trend in wear resistance. The base sample S0 has the highest wear rate (4.8 $mm^3/N{\cdot}m$) and mass loss (18.5 mg), and the optimized sample S15 has the lowest (0.9 $mm^3/N{\cdot}m$ and 4.9 mg, respectively). The intermediate samples (S3, S6, S9) also show substantial decreases, indicating the positive influence of reinforcement distribution and processing. A minor variation is seen in samples S4 and S7, but the overall trend shows that improvement in tribological properties of the composite can be obtained with the addition of SiC and Gr. The degradation process of both parameters reflects the better integrity of the surface, the lower amount of material removal, and the better load-bearing capacity for the material composite.

3.5. Identification of Best Performing Composite

Based on the experimental results, the 82 wt.% Al6061, 15 wt.% SiC, and 3 wt.% Gr composition is observed as the most optimal mix in terms of overall performance with all the output parameters. This composite has greater hardness, tensile strength, increased wear resistance, and balanced ductility. Further, the microstructural analysis is carried out for this composition to examine the morphological characteristics of the composite.

3.6. Microstructural Analysis

3.6.1. Optical Microscopy

Figure 16 demonstrates the optical microscopy pictures of (a) the base Al6061 alloy and (b) the hybrid composite with 82 wt.% Al6061, 15 wt.% SiC, and 3 wt.% Gr at a scale of 100 µm. Figure 16(a) shows that the base alloy microstructure has relatively coarse and equiaxed grains with well-defined grain boundaries, which is typical of Al6061 that has been conventionally processed. Comparatively, the composite microstructure of Figure 16(b) shows a finer grain structure in addition to the existence of a hybrid reinforcement particle distributed in the aluminum matrix. The darker areas are related to the combined SiC and Gr reinforcements, which are seen to be embedded along grain boundaries as well as inside the grains. These reinforcements enhance grain refinement and inhibit grain growth during solidification, resulting in a smaller, homogenous microstructure. This fine structure will improve mechanical characteristics like hardness and strength, where the Gr phase will help to improve the tribological characteristics.

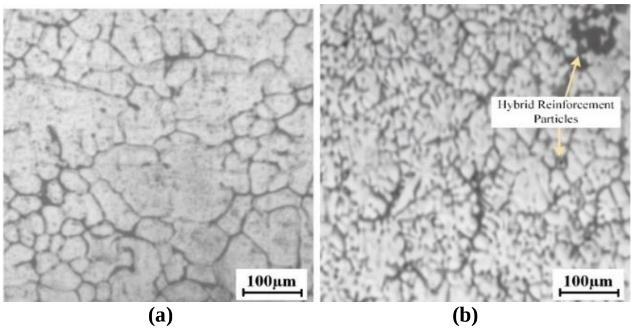

(a) (b)

Fig. 16 Optical Microscopy Images of (a) Base Alloy (b) Composition of 82 wt.% Al6061, 15 wt.% SiC, and 3 wt.% Gr

3.6.2. Scanning Electron Microscopy (SEM)

The SEM micrographs of (a) the unreinforced Al6061 alloy and (b) the hybrid composite (82 wt.% Al6061, 15 wt.% SiC, and 3 wt.% Gr) are depicted in Figure 17 at a scale of 20 µm. The microstructure of the base alloy (a) is relatively uniform and has clearly observable porosity and microcracks, which may have developed due to solidifying or processing. Conversely, the composite micrograph (b) shows clearly the presence of the dispersed SiC particles and Gr phases embedded in the Al matrix as small clusters. The SiC particles are observed as bright, irregularly shaped reinforcements, and the Gr is observed as darker and flake-like appearances. Even though minor porosity can be observed, the general microstructure shows effective incorporation and placement of the reinforcements in the matrix. The hard SiC particles and solid lubricant Gr make the hybrid composite better than the base alloy in terms of load-bearing capacity and wear resistance.

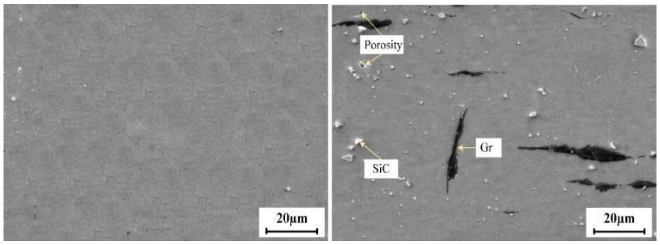

(a) (b)

Fig. 17 SEM Images of (a) Base Alloy (b) Composition of 82 wt.% Al6061, 15 wt.% SiC, and 3 wt.% Gr

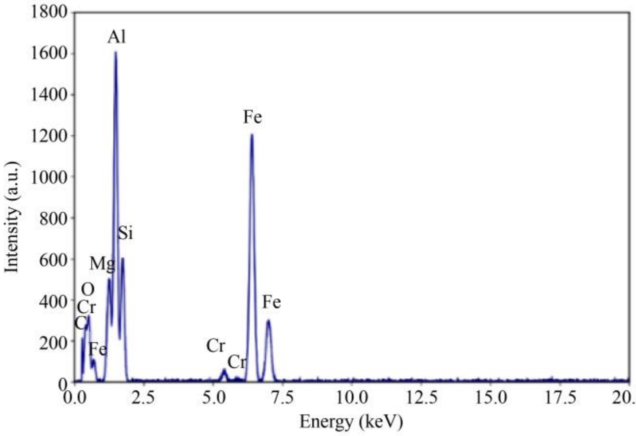

Fig. 18 EDS Plot for the composition of 82 wt.% Al6061, 15 wt.% SiC, and 3 wt.% Gr

3.6.3. Energy Dispersive Spectroscopy (EDS)

Figure 18 shows the EDS spectrum of the hybrid composite with 82 wt.% Al6061, 15 wt.% SiC, and 3 wt.% Gr. The spectrum reveals a strong Al peak, which proves that Al6061 is the major matrix phase of the composite. The silicon (Si) peaks are a confirmation of Si reinforcement in the form of SiC. The presence of Gr particles in the matrix is indicated by the presence of carbon (C) peaks. Additionally, minor peaks are also detected that contain magnesium (Mg), iron (Fe), chromium (Cr), and oxygen (O), which are typical alloying elements and trace elements in Al6061. The high intensity of the Al peak is due to the higher weight percentage of Al in comparison with the other elements present in the composition. In general, the EDS analysis indicates the efficient incorporation and adequate distribution of Al, SiC, and Gr in the hybrid composite without traces of undesirable contaminant elements.

3.6.4. X-Ray Diffraction (XRD)

Figure 19 shows the X-ray diffraction (XRD) pattern of the hybrid composite (i.e., 82 wt.% Al6061, 15 wt.% SiC, and 3 wt.% Gr). The observed diffraction peaks of about 38°, 45°, and 65° are attributed to the (111), (200), and (220) crystal planes of the face-centered cubic (FCC) Al matrix, indicating that the Al6061 is still the dominant phase in the composite. The intensity of the (111) peak is high, and this means that the preferred orientation of the Al phase is high. Along with the Al peaks, the SiC and Gr reinforcements are determined by their typical diffraction patterns, which show that the ceramic and solid lubricant phases are successfully introduced into the matrix. The fact that there are no additional sudden peaks means that no undesirable intermetallic compounds or second phases were created during the stage of the processing, which means that there is a high phase stability and compatibility between Al6061, SiC, and Gr. In general, the XRD data confirms the presence of multiple phases and correct distributions of reinforcements in the Al matrix composite.

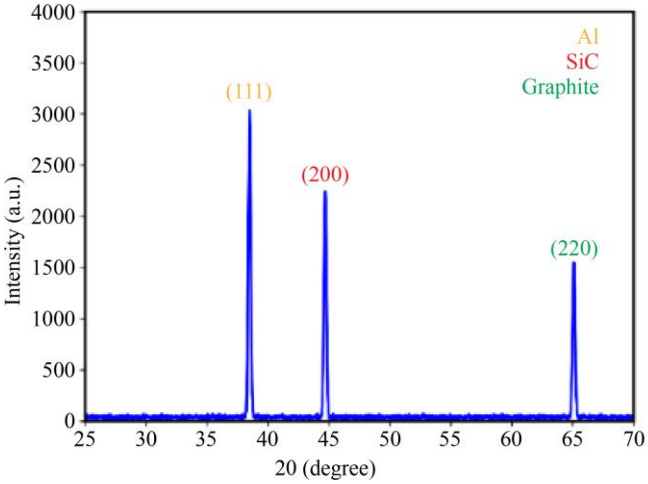

Fig. 19 XRD Plot for the composition of 82 wt.% Al6061, 15 wt.% SiC, and 3 wt.% Gr

3.7. Prediction Outcomes

Figure 20 provides a comparative violin plot analysis of the predicted density values of the proposed model and other existing models, such as RF, SVR, DT, LR, and MLP, versus the actual density distribution. The density of the proposed model agrees with the actual data, almost in terms of median and spread, which means high prediction accuracy and consistency. Conversely, the RF, SVR, DT, and MLP models exhibit a smaller dispersion from the actual values, which implies that these models are less precise in prediction. The LR model evidences more variance in its spread with the actual values. In general, the suggested model is the most accurate in terms of matching the actual density distribution, which proves its advantageous position in a more precise prediction of material density than the traditional ML models.

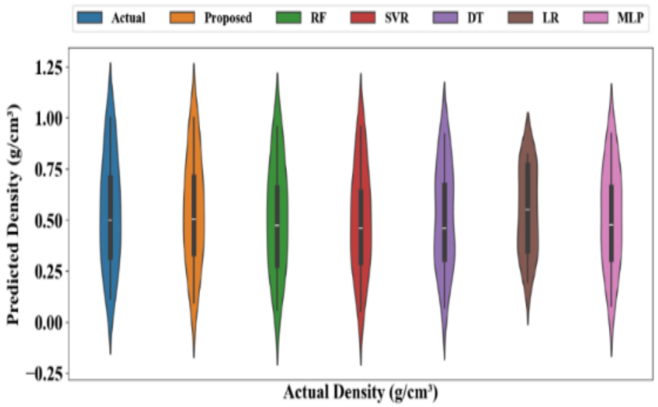

Fig. 20 Comparative Analysis of Density with Proposed and Other Existing Models

Figure 21 shows the comparative violin plot of the actual porosity distribution versus the predicted porosity values of the proposed model, RF, SVR, DT, LR, and MLP. The suggested model illustrates a distribution that is very close to the real data on porosity, and the median is the same, and the spread is relatively compact, which implies it shows high predictive quality and consistency. Although models such as SVR and RF demonstrate relatively similar density distributions, the other existing models, including DT and MLP, demonstrate stronger distortions in the shapes of the probability densities. The LR model exhibits a larger dispersion variation with the actual values. In general, the suggested model demonstrates the highest correspondence with the real porosity distribution and is better than the other models regarding accuracy and reliability in predicting porosity.

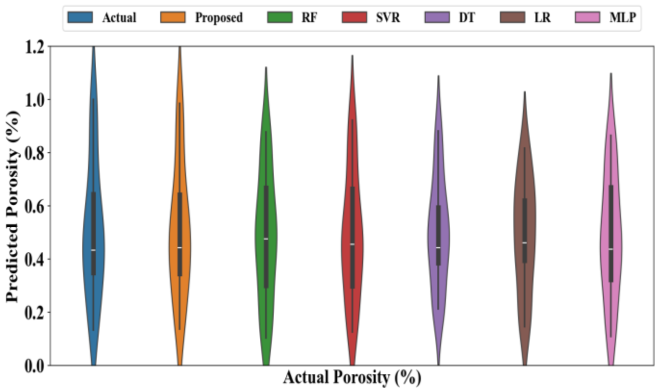

Fig. 21 Comparative Analysis of Porosity with Proposed and Other Existing Models

A comparative violin plot of the actual and the predicted VHN distribution of various models, including proposed, RF, SVR, DT, LR, and MLP, is shown in Figure 22. The suggested model reflects a similar central tendency and spread, which represents a more pronounced prediction faithfulness and improved generalization. The RF, SVR, DT, and LR models show a high variance with the real value, which implies that they have lower predictive capabilities. The MLP model performs moderately, but it has more variability than the suggested approach. All in all, the findings indicate that the suggested model has high predictive consistency and reliability in the real VHN distribution compared to traditional ML models.

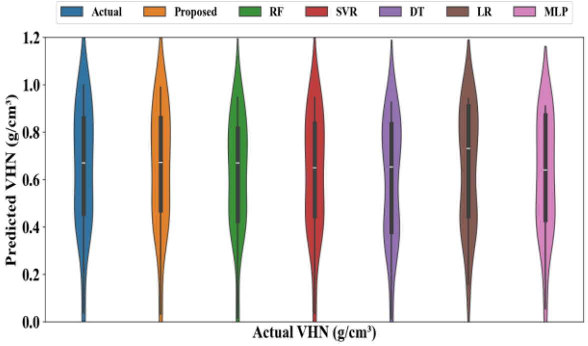

Fig. 22 Comparative Analysis of VHN with Proposed and Other Existing Models

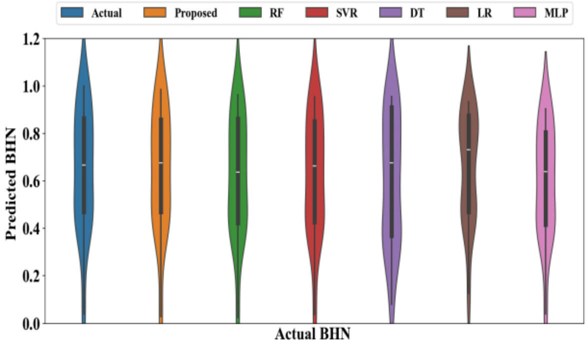

Fig. 23 Comparative Analysis of BHN with Proposed and Other Existing Models

Figure 23 depicts the violin plot comparison between the actual BHN distribution and the predicted BHN values generated by the proposed RF, SVR, DT, LR, and MLP. The proposed DADNN model presents the most similarity to the real distribution of BHN since the median value, interquartile separation, and the shape of the violin are the same, depicting that the hardness behavior is correctly modeled. The models RF and SVR exhibit a very minimal deviation from the actual value; however, they offer a better performance with a small prediction error. The DT model fits the central tendency fairly well but has a greater variability, indicating unstable predictions. LR exhibits a pronounced movement to lower values of BHN and larger dispersion, which is underfitting and has less predictive ability. The MLP model shows a moderate performance, but its distribution is wider than that of the suggested method. In general, the result indicates that the DADNN model generates a higher level of consistency and predictive accuracy in estimating the BHN than the traditional ML models.

The comparison of the violin plot of the actual YS distribution and the predicted values of the proposed RF, SVR, DT, LR, and MLP models is shown in Figure 24. The offered model demonstrates the highest level of similarity with the real yield strength distribution, and the medians, interquartile range, and general density structure are almost equal, which indicates the higher ability of the proposed model to characterize the real mechanical performance. The models SVR and RF exhibit slight variations in density concentration near the median when compared to the actual measurements. The DT model estimates the central tendency but slightly shows a wider dispersion and a slight skewness, indicating varying predictions. LR shows a strong bias towards lower yield strength values and high dispersion, representing a lack of flexibility in modeling and underfitting. The MLP model works better than the LR but still has a broader variability than the proposed approach. In general, the findings prove that the proposed model yields the most precise and consistent YS prediction among the considered ML strategies.

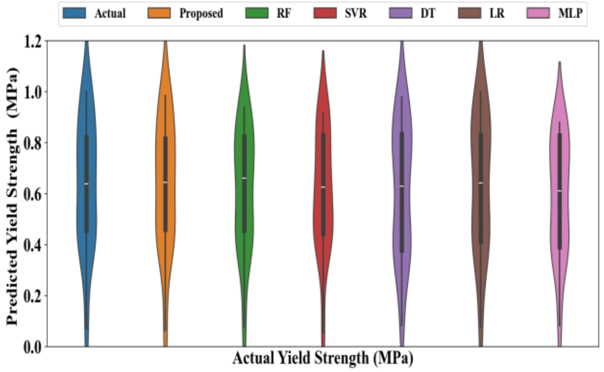

Fig. 24 Comparative Analysis of YS with Proposed and Other Existing Models

Figure 25 presents the violin plot comparison between the actual UTS values and the predicted UTS values produced by the proposed RF, SVR, DT, LR, and MLP models. The suggested model shows the greatest similarity with the observed UTS distribution, with almost the same median, interquartile range, and general density distribution, which suggests that it is more capable of capturing the tensile strength features. The RF and SVR models show varying degrees of fluctuation in their density widths, particularly near the median and the tails of the distribution. The DT model presents both a wider distribution and a small off-the-real distribution, which indicates moderate prediction ability. The LR approach exhibits a strong tendency to the lower UTS values and the increased dispersion, indicating underestimation and the lack of representational power. The MLP model has better performance than the LR, but still has a wider variability than the proposed approach. In general, the findings demonstrate that the proposed model provides an increased predictive power and stability in UTS estimation, in comparison with the traditional ML approaches.

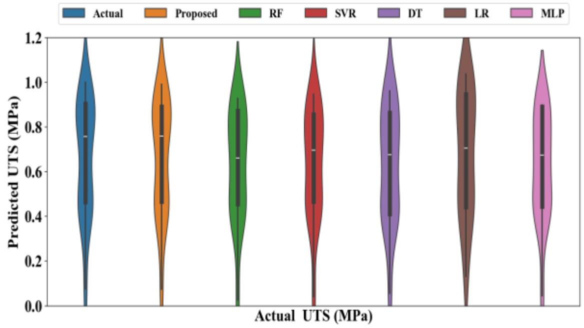

Fig. 25 Comparative Analysis of UTS with Proposed and Other Existing Models

Figure 26 presents the violin plot comparison of the actual percentage elongation distribution and the predicted percentage elongation values of the proposed, RF, SVR, DT, LR, and MLP models. The proposed model reveals the best fit to the real distribution in terms of a similar median value, interquartile range, and the overall shape of the density, showing that it is highly effective in imitating the ductility performance. The RF model exhibits minor deviations from the actual values, which indicates a minor deviation in predictions. The SVR model is consistent with the general trend of the actual values, but they extend to larger tails, which means there are cases of overestimation or underestimation. The DT model has a clear tendency to provide lower elongation values with a narrower spread, which indicates underestimation and less predictive stability. The LR model depicts larger dispersion and modest overestimation in the high range, which means that the elongation characteristics are not consistently modeled. The MLP model has a moderate performance, which approximates the central tendency but still shows more variability than the suggested approach. On the whole, the findings prove that the proposed model is the most precise and predictable in terms of percentage elongation among all the other ML methods.

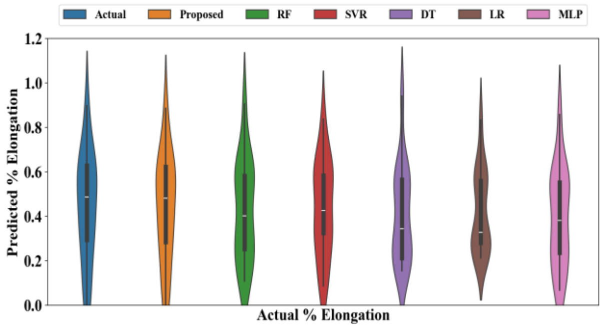

Fig. 26 Comparative Analysis of Elongation with Proposed and Other Existing Models

Figure 27 shows the violin plot comparison of the actual wear rate and the predicted wear rate values of the proposed RF, SVR, DT, LR, and MLP models. The proposed model demonstrates the most similarity with the real distribution of wear rates, which means that it is highly able to model tribological behavior. The SVR model and the RF model have small differences in their density concentrations, especially around the tails and the median, implying the presence of variations in the predictions. The DT model conveys the central tendency fairly well but with a narrower range, indicating a small range of variation.

On the contrary, the LR model shows a clear upward movement with a wider dispersion, which means overestimation and decreased predictive capability. The median of the MLP model is also bigger and broader in comparison with the actual data, which indicates moderate deviation. Overall, the findings reveal that the proposed model is the most accurate and stable when it comes to predicting the wear rate compared to the other traditional ML methods.

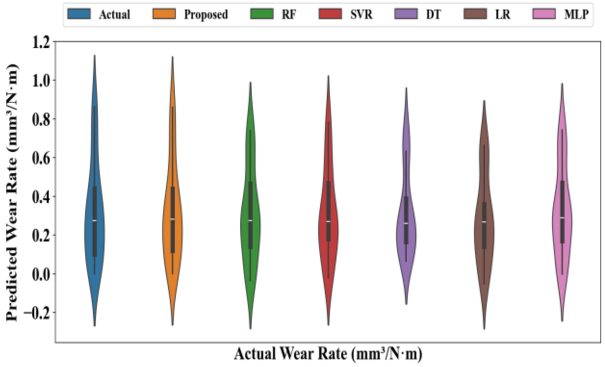

Fig. 27 Comparative Analysis of Wear Rate with Proposed and Other Existing Models

Figure 28 shows the violin plot comparison of the actual distribution versus the predicted mass loss values produced by the proposed model, RF, SVR, DT, LR, and MLP models. The proposed model demonstrates the most similarity with the real distribution of mass loss, where the median, interquartile, and overall shape of the density are almost the same, which means that the material degradation is properly captured by the proposed model. The RF and SVR models show a slightly wider distribution from the actual data, even though they exhibit reasonably accurate predictions. The DT model estimates the central tendency but with slightly narrower dispersion, indicating that it has a lower representation of variability. The LR model shows an evident upward movement and much wider dispersion as compared to the real data, as it overestimates and reduces predictive accuracy. Median values and differences in the MLP model are also larger and more varied than the actual, and this is evidence of moderate deviation. In general, the findings prove that the proposed model is the most realistic and reliable in predicting mass loss in comparison with the other traditional ML models.

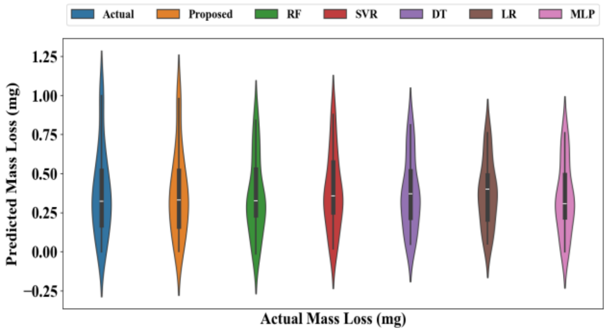

Fig. 28 Comparative Analysis of Wear Rate with Proposed and Other Existing Models

3.8. Statistical Significance Testing

The significance of the performance improvements made by the proposed DADNN-iCSOA framework has been evaluated using statistical testing and compared with the conventional machine learning models. The prediction errors of the LR, DT, SVR, RF, MLP, and proposed models were used to perform the paired t-tests. The null hypothesis (H_0) stated that there was no statistically significant difference between the proposed model and the comparison model, while the alternative hypothesis (H_1) assumed that the proposed models had better performance than the comparison models. The p-values obtained in all the comparisons were less than the set threshold value of 0.05, which showed that the proposed model improved significantly.

Table 9 shows the statistical significance analysis of the proposed DADNN-iCSOA model and existing machine learning models based on the t-test evaluation. The obtained results of the proposed DADNN-iCSOA model were found to be statistically significant with t=2.22, p=0.001. Additionally, the typical models like LR, DT, SVR, RF, and MLP produced statistically significant results with all the p-values being below 0.05. LR had the highest t-value compared to other models used, which were DT (4.92), SVR (4.11), RF (3.42), and MLP (2.88). The small p-values indicate that the performance differences between the models are not significant, which further validates the efficiency and reliability of the proposed DADNN-iCSOA framework in predictive analysis.

Table 9. Statistical Significance Analysis Using Paired t-Test

Model	t-value	p-value	Statistical Significance
Proposed DADNN-iCSOA	2.22	0.001	Significant
LR	5.84	0.002	Significant
DT	4.92	0.003	Significant
SVR	4.11	0.005	Significant
RF	3.42	0.009	Significant
MLP	2.88	0.017	Significant

3.9. Training and Testing Loss

The curve of training loss and testing loss with respect to epochs during the process of training the model is shown in Figure 29. Initially, both losses are relatively high, indicating that the model is in the early learning stage. The loss values decrease significantly as the epoch number grows, indicating good learning and performance. The training loss slowly decreases until it reaches around 0.03, and the testing loss slowly decreases until it reaches around 0.03–0.04. The training and testing loss curves are closely aligned, suggesting that the model is not overfitting the training data and can be expected to perform well on new data. The fluctuations seen in testing loss at later epochs are minor and expected and can be caused by different variations in the validation samples. The agreement between both curves at lower values of loss confirms the good stability, reliability, and predictive ability of the developed model.

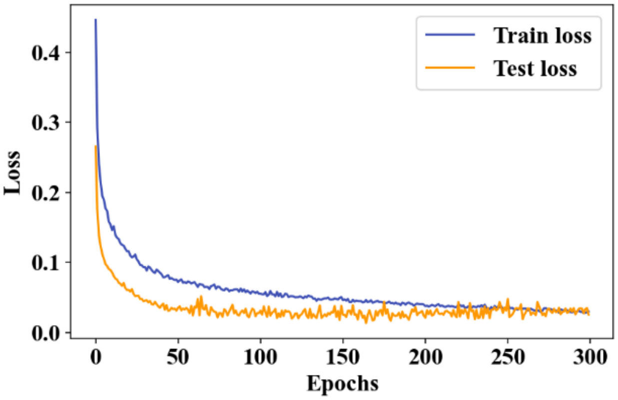

Fig. 29 Training and Testing Loss vs Epoch

3.10. Evaluation of Performance Metrics

Figure 30 (a) shows a comparison between the radial plot of the Mean Absolute Error (MAE) of the proposed model and the standard ML methods, such as RF, SVR, DT, LR, and MLP. The suggested model with the lowest MAE value (0.012) indicates a significantly higher prediction accuracy and a very small deviation from the true values. Under the methods of the baseline, the RF (0.058) and SVR (0.071) have moderate levels of errors, but the MLP (0.098) and DT (0.112) have higher prediction errors. The LR model has the highest MAE (0.124) and indicates its low ability to capture the nonlinear relationships in the data. The gradually increasing radial lengths indicate the variation in performance, which validates the higher predictive accuracy and strength of the proposed model compared to the traditional regression methods.

Figure 30 (b) shows the radial chart of comparative performance analysis by the Root Mean Square Error (RMSE) of various predictive models, such as the proposed, RF, SVR, DT, LR, and MLP. The proposed model has been observed to be the most precise of all other tested algorithms, with a considerably low RMSE of 0.015. Conversely, the baseline models have gradually increasing error rates, with the highest error rates of 0.080 and 0.150 for the RF and SVR, respectively. The MLP and DT remain below with a performance of 0.240 and 0.420, respectively, whereas LR has the lowest accuracy with the least RMSE value of 0.560. Such findings indicate the usefulness of the suggested method in reducing prediction error in relation to classical ML methods.

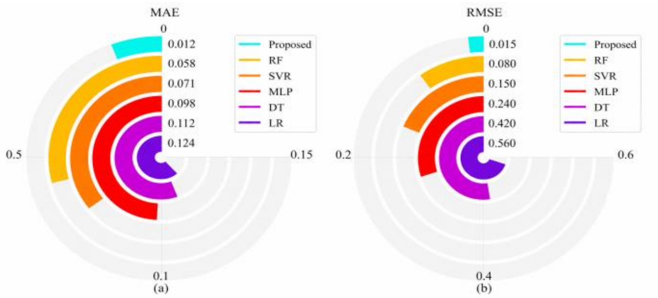

Fig. 30 Performance Metric Evaluation (a) MAE (b) RMSE

A comparative analysis of model performance according to the Mean Squared Error (MSE) is presented in the radial bar chart in Figure 31 (a). The suggested model has the lowest MSE of 0.0009, which implies a high predictive quality and a low error. RF comes next with an MSE of 0.0011 and is relatively strong-performing with a slightly higher error than the proposed approach. The MSE of SVR and MLP is 0.0018 and 0.0026, respectively, which indicates moderate prediction error. DT has an MSE of 0.0038, and LR has the largest error of 0.0050, which shows that it has a relatively low predictive ability. Together, these findings support the fact that the proposed model outperforms the conventional ML models in terms of prediction accuracy and error minimization.

Figure 31(b) demonstrates a comparative evaluation of the R^2 score of different models in terms of a longer bar stretching towards the value of 1, indicating the better predictive power. The proposed model has almost perfect correlation with the outstanding R^2 of 0.998, which outperforms any other baseline algorithm. After the suggested model, the SVR and the RF models perform very well with a score of 0.935 and 0.964, respectively. The MLP and DT models come next with scores of 0.915 and 0.892. Lastly, the LR model has the least predictive accuracy with an R^2 score of 0.872. These findings indicate that the proposed model offers an increased predictive accuracy over the traditional ML models.

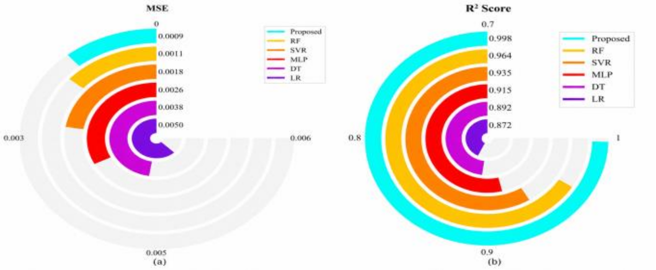

Fig. 31 Performance Metric Evaluation (a) MSE (b) R^2

Figure 32 (a) is a radial bar chart that compares the models by the Mean Absolute Percentage Error (MAPE), in which a smaller radial bar indicates a smaller percentage of error and a higher predictive reliability. The proposed model has the best accuracy with an MAPE of 0.143, which is much higher than the other baseline algorithms. The RF and SVR models exhibit moderate errors of 0.246 and 0.346, respectively. The MLP and DT models have performance lowering to 0.457 and 0.664, respectively. The LR model has the largest error in this measure with a MAPE of 0.712, and therefore, it is not the best model in making accurate percent-based predictions. The results are again consistent with the other metrics of errors, which support the overall strength of the proposed model in all performance indicators.

Figure 32 (b) shows the Standard Deviation of Error (SDE) of different models, with a shorter bar corresponding to a more stable and predictable model. The proposed model has the best degree of accuracy with an SDE of 0.011, indicating that the error of prediction is well concentrated and predictable. The other models that come next are the RF and the SVR, with low SDE values of 0.018 and 0.021, respectively. The values of the MLP and DT are moderate at 0.032 and 0.047 when the radial bars are extended. The highest variability of the results in the LR model was observed, which provides the highest SDE value of 0.065. These findings also confirm the strength of the suggested model, proving that it not only decreases the total error but also has better consistency than contemporary ML methods.

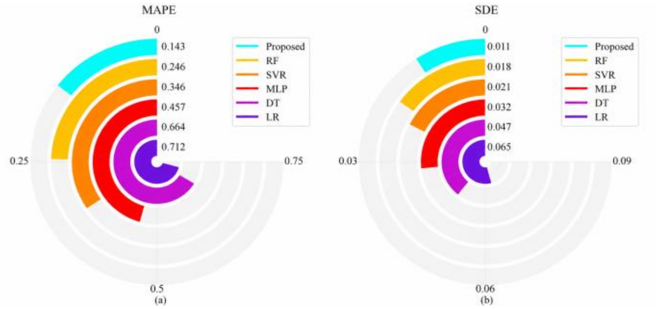

Fig. 32 Performance Metric Evaluation (a) MAPE (b) SDE

3.11. Error Distribution Analysis

3.11.1. Physical Properties

The error distribution for each sample index for different ML models, including the proposed, RF, SVR, MLP, LR, and DT models, is shown in Figure 33. The most consistent and stable performance is shown in the proposed model, with its error fluctuating around a near-zero value across the samples. The conventional models, on the other hand, show greater scatter of the error values, especially between sample numbers 10-11 and 15-21. The LR is the most unstable model, with extreme negative deviations of nearly -70%, which result in poor prediction reliability. Likewise, there are significant positive spikes in the errors for SVR, RF, MLP, and DT, particularly around sample index 10, where the errors are more than 30-50%. The overall results show that the proposed strategy is more robust and accurate in the prediction of errors than the existing ML methods.

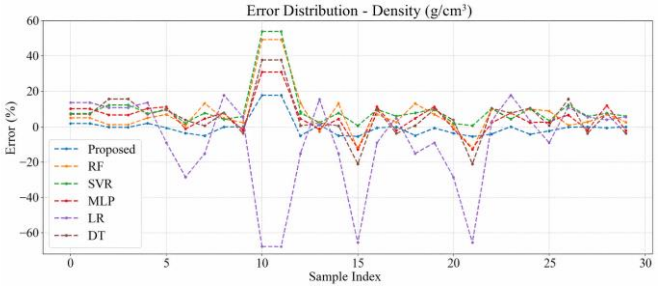

Fig. 33 Error Distribution of Density

The error distribution of the proposed model and ML methods (RF, SVR, MLP, LR, and DT) for the prediction of porosity at different sample indices is displayed in Figure 34. The error values of the proposed method are very small and nearly stable for all the samples, which proves the strong consistency and robustness of the method in predicting the results. The conventional models, on the other hand, demonstrate large variations in the errors across the data set. Moderate positive and negative deviations are shown in RF, SVR, and MLP, and errors often range between -10% and 20%. The LR model also shows an unstable response with significant oscillations over multiple sample indices. The DT model yields the highest differences, up to almost −65% at certain sample indices, indicating that the model generalizes poorly and has unstable predictions. In general, it indicates that the proposed method significantly reduces prediction errors and yields a more accurate estimation of porosity than the current ML models.

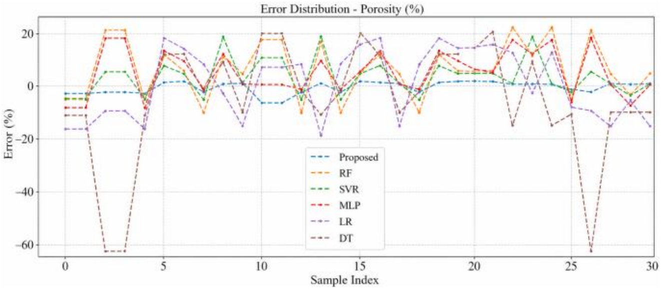

Fig. 34 Error Distribution of Porosity

3.11.2. Mechanical Properties

Figure 35 shows the distribution of errors of the VHN prediction for various sample indices with the proposed and the existing ML methods, such as RF, SVR, MLP, LR, and DT. The Proposed approach shows the least fluctuations in the error values over the extended period, showing that there is high confidence in prediction and low error variance. The conventional models, on the other hand, show significant variations in error values at various sample indices. The MLP model has substantial negative errors around sample index 10-11, whereas the RF and DT models have large positive deviations (more than 50%). The LR model shows the highest level of instability with extreme negative deviations reaching to values as high as -100%, which shows a lack of consistency in predicting. The performances under SVR are relatively better than the other traditional methods and also a moderate oscillations in error value is observed. Overall, the results clearly indicate that the proposed method effectively reduces the prediction errors and gives better robustness and stability in predicting VHN than all the existing ML models.

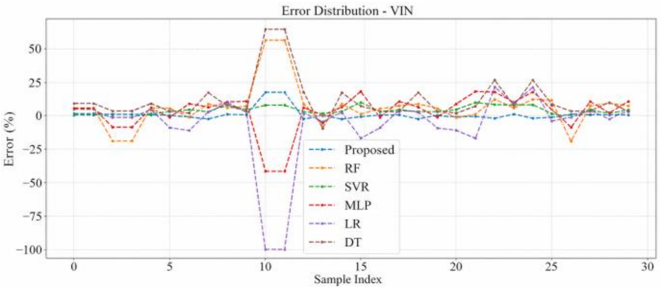

Fig. 35 Error Distribution of VHN

The analysis of error distribution for different ML models for BHN prediction over the various sample indices is presented in Figure 36. The proposed model and the other approaches, such as RF, SVR, MLP, LR, and DT, are evaluated. The proposed method has relatively small and stable error values across samples, reflecting strong prediction consistency and robustness. Large fluctuations are observed for both RF and DT with sharp positive and negative deviations, especially in the vicinity of sample indices 10 and 11, where the error drops drastically. LR also has a few error peaks, but they are negative, whereas MLP and SVR have moderate performance with relatively controlled error variations. The proposed model performs better than the conventional models as it provides minimum error dispersion and better prediction reliability, making the model more effective for accurate BHN estimation.

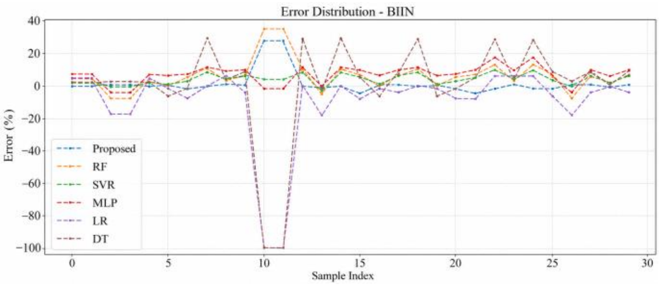

Fig. 36 Error Distribution of BHN

The error distribution graph for YS prediction for various sample indices is given in Figure 37. It can be seen that the proposed model outperforms RF, SVR, MLP, LR, and DT models in terms of its prediction stability and consistency across all sample indices. The proposed approach has a very small deviation from the zero error line, which infers that the prediction is very accurate and there is a very small deviation from actual values. However, the positive and negative error variations are greater in the existing models, especially at the sample indices around 3, 10-15, and 25-27, where the deviations of LR and DT are much greater. Moderate fluctuations are observed in RF and SVR, and inconsistent behavior is observed in MLP with repeated peaks. Overall, the proposed model has good robustness and can effectively reduce the prediction error in the estimation of YS.

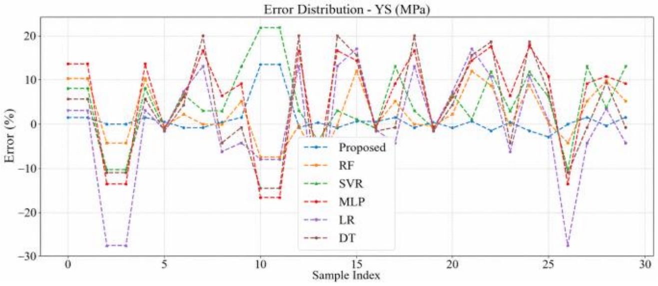

Fig. 37 Error Distribution of YS

Figure 38 shows the error distribution analysis of UTS for the proposed model, and other models such as RF, SVR, MLP, LR, and DT. It is observed that the proposed model has a very low error variation and highly accurate predictions across the data set. The proposed approach stays very close to the zero-error line for almost all the samples and shows high generalization power and prediction stability. The traditional models, on the other hand, show significant variability and extreme deviations. The stable prediction behavior is highlighted by large positive fluctuations around sample indices 10-12 for RF, SVR, and MLP, whereas severe negative deviations for LR in excess of -60% highlights unstable prediction behavior. DT also shows some irregular oscillations across multiple samples. The error spread in the proposed model is less compared to the existing ML models, which shows the effectiveness in estimating UTS accurately.

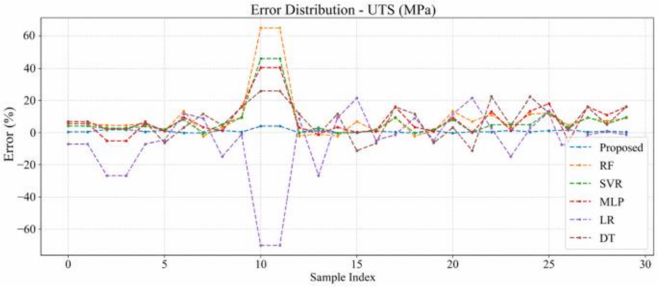

Fig. 38 Error Distribution of UTS

Figure 39 presents the % elongation error distribution of the proposed model, along with the models such as RF, SVR, MLP, LR, and DT. The proposed model consistently performs better than the other comparative models with smaller error magnitudes for most sample indices. A few variations still appear, but the proposed approach is generally more stable and near the zero error reference line. RF, SVR, MLP, LR, and DT show significant positive and negative deviations, with some models achieving values around -100% error at a few sample indices (around 8 and 23). LR and DT exhibit unstable behaviour with large oscillations and prediction errors. The overall trend points out that the proposed model can greatly enhance the accuracy of prediction and decrease the estimation errors in percentage elongation analysis.

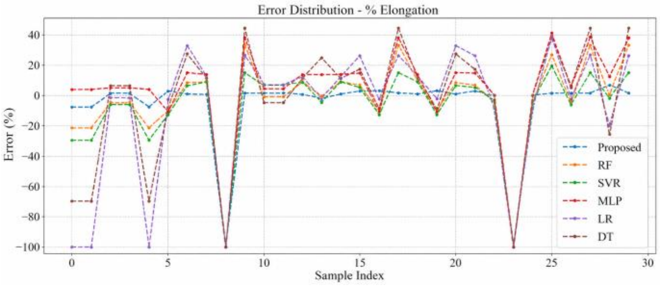

Fig. 39 Error Distribution of % Elongation

3.11.3. Tribological Properties

Figure 40 presents the wear rate error distribution plot of different models, including the proposed, RF, SVR, MLP, LR, and DT. The proposed model has comparatively lower prediction errors and smoother error transitions compared to other existing models. The proposed method keeps the errors in the close vicinity of the zero line for most of the samples, thereby demonstrating its stable and accurate prediction of the wear rate. On the other hand, RF, SVR, MLP, LR, and DT show sudden jumps and high variation in errors, with a few samples showing very high errors, both positive and negative, approaching ±100%. These differences suggest a lack of consistency and weakness in the traditional models. In particular, around the sample indices of 5, 16, and 19, the behavior of RF and LR is very irregular. Thus, the proposed model provides more stability in prediction and more reliability in wear rate estimation.

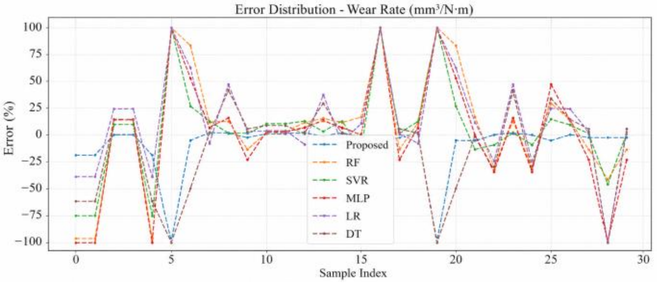

Fig. 40 Error Distribution of Wear Rate

The error distribution plot of the mass loss between the proposed, RF, SVR, MLP, LR, and DT models is given in Figure 41. The proposed model has the most accurate and balanced prediction performance among all the models compared. The proposed approach shows very little deviation from the zero-error baseline and has uniform prediction behavior throughout the range of the sample. In contrast, RF, SVR, MLP, LR, and DT show substantial variations with multiple peaks and valleys. RF has large positive peaks at sample indices 5, 16, and 19; several models have extreme negative values at certain samples close to -100%. Lower prediction consistency is also obtained for LR and DT with unstable oscillatory patterns. In general, the proposed model is more robust, has lower prediction error, and is more capable of estimating the mass loss values.

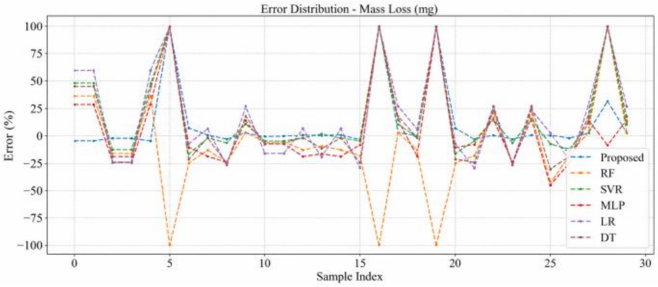

Fig. 41 Error Distribution of Mass Loss (mg)

3.12. Prediction Uncertainty Analysis

The confidence and prediction interval plot for density shown in Figure 42 (a) demonstrates a highly accurate relationship between the actual and predicted values. The data points are mostly concentrated near the diagonal regression line, suggesting that the model performs well in predicting the data and has a low level of deviation. The relatively small confidence interval indicates that the regression estimation is stable and reliable, but the prediction interval is wide enough to reflect the variability of the observed data. There are only a few points with small deviations at the lower and upper density limits, which are indications of a very small prediction error. Overall, the findings validate that the model has excellent generalization and density estimation capabilities and that the overall accuracy is very reliable throughout the entire data set.

The confidence and prediction interval plot for porosity shown in Figure 42 (b) illustrates a strong correlation between the actual and predicted porosity values. Most of the data points cluster around the fitted regression line, indicating that the model accurately represents the relationship between the data. The prediction interval covers the variations of the observed samples, while the confidence interval covers the regression predictions with high confidence across the range. There are slight differences at the boundary values, but they have little impact on the accuracy of the prediction. The results show that the proposed method gives high prediction accuracy for porosity, along with low estimation error and good prediction consistency.

Figure 42 (c) illustrates the VHN confidence and prediction interval plot, which shows a good agreement between the actual values and the predicted values obtained from the proposed model. The points are tightly clustered on the regression line, showing that the model provides good prediction accuracy and very little residual error. The narrow confidence interval indicates high strength and stability of the regression estimation, while the wide prediction interval reflects the variation of the individual observations. There are only a few samples at the extremes that fall slightly off the fitted line, suggesting very low prediction uncertainty. In general, the results show that the offered model can predict VHN with high precision, consistency, and strong generalization.

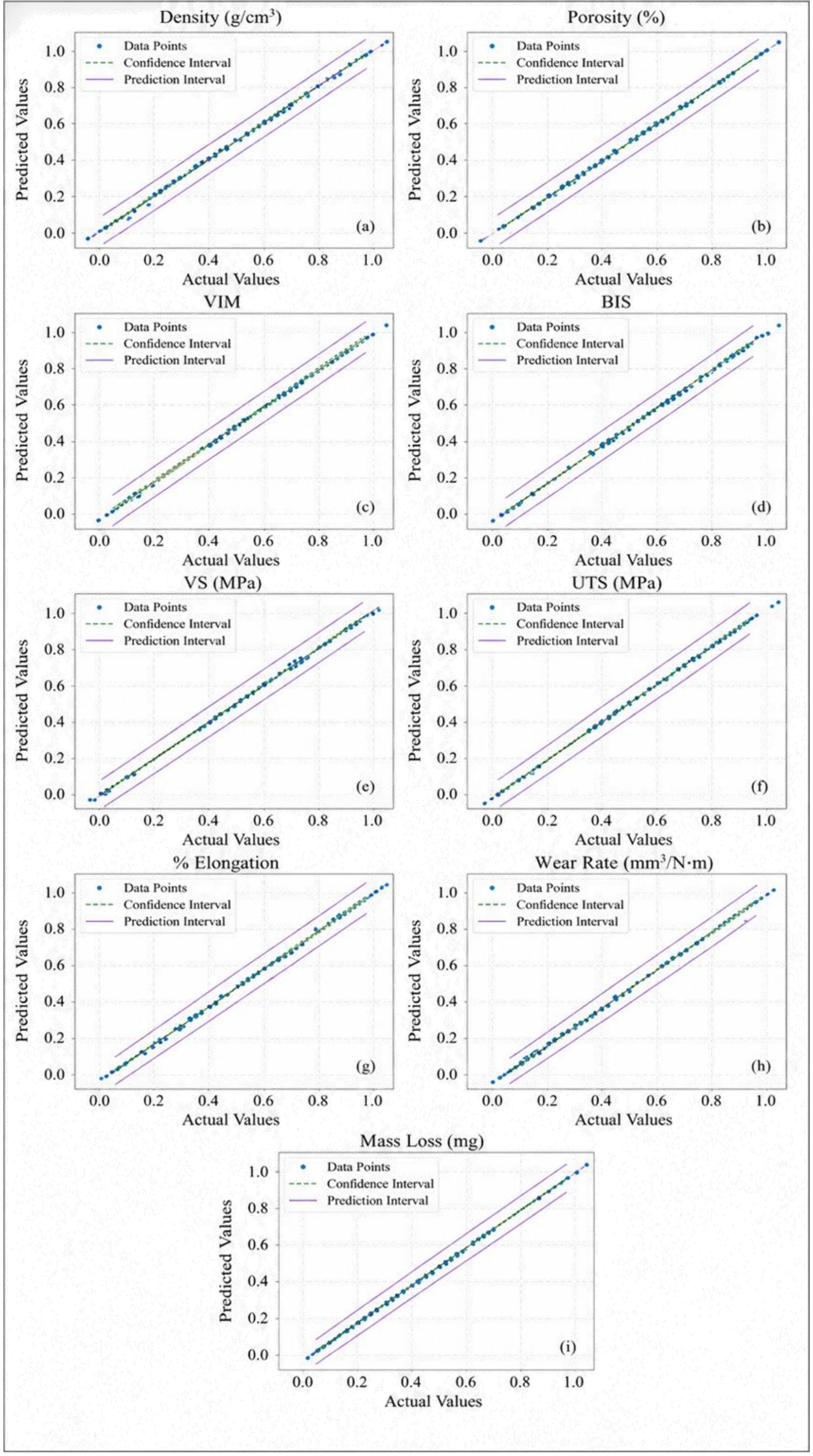

Fig. 42 Confidence and Prediction interval plots (a) Density (b) Porosity (c) VHN (d) BHN (e) YS (f) UTS (g) % Elongation (h) Wear Rate (i) Mass Loss

The plot of the confidence and prediction intervals for BHN given in Figure 42 (d) shows a very linear relationship between the actual and predicted values, indicating the ability of the proposed prediction model. The data points are generally close to the regression line, suggesting a low estimation error and good prediction capabilities over the full range of values. The confidence interval is narrow, indicating that the predictions from the model are reliable and consistent, while the prediction interval covers the range of experimental data. An excellent predictive stability is confirmed by the overall distribution, although there are minor deviations near the higher BHN values. Therefore, the proposed model can predict BHN with a good regression capability and high accuracy.

Figure 42 (e) presents the correlation of predicted values and actual values for the proposed model for YS; the plot of the model shows a very good correlation between predicted and actual values. Most of the data points lie very close to the regression line, suggesting that the predictions are accurate and there is little variation across the data points. The confidence interval is narrow throughout the range, which indicates that the regression estimate is highly reliable and consistent. Moreover, the prediction interval accounts for the variability of observations with a limited spread. There are only minor deviations at the lower and higher YS values for a few samples, indicating very low prediction uncertainty. In general, the findings show that the proposed model delivers accurate and reliable predictive performance for YS.

The confidence and prediction interval plot for UTS, shown in Figure 42 (f), illustrates excellent agreement between the actual and predicted values. The closeness of the data points to the fitted regression line shows that the proposed model is capable of estimating UTS with very low residual error. The narrow confidence interval assures robustness and stability in the regression analysis, and the prediction interval is broad enough to cover the variation in the experimental observations. A few values slightly deviate at the highest end, but overall, the distribution is very linear and consistent. The results show that the proposed method can predict the UTS accurately and reliably with good generalization ability and high predictive consistency.

Figure 42 (g) represents the confidence and prediction interval plot of % elongation, which indicates that the actual and predicted data values of the proposed model have a very good relationship. The dots are tightly clustered around the regression line, suggesting the model has a high predictive ability and very small estimation error. The narrow confidence interval suggests a high degree of reliability and consistency in the regression model, whereas the prediction interval adequately reflects the variability in the experimental observations. The distribution is very linear and stable, with slight deviations seen at the extremes. The obtained results indicate that the proposed model can predict the percentage elongation with high precision, robustness, and good generalization.

The confidence and prediction interval plot for wear rate shown in Figure 42 (h) indicates that the actual values are closely aligned with the predicted values, highlighting the accuracy of the proposed prediction method. The points are very close to the regression line, showing that the model is a good fit and that the residuals are small for most of the data. The confidence interval is still narrow, indicating the stability and reliability of the regression estimation, while the prediction interval covers the variability of the individual observations. The data points slightly deviate at the lower and upper ranges, but the general trend shows a very linear relationship between the values for the actual and predicted wear rates. Thus, the results confirm the ability of the model to predict the wear rate with acceptable accuracy and low uncertainty.

The confidence and prediction interval plot of mass loss, presented in Figure 42 (i), illustrates a high degree of correlation between the actual and predicted values from the proposed model. Most of the data lie very close to the regression line, which means that predictions are very accurate, and there is little estimated error in the predictions throughout the data. The confidence interval is relatively narrow in the entire range, indicating robustness, stability, and reliability of the regression analysis.

Besides, the prediction interval covers most of the variations in the observed data with a limited dispersion. Very few deviations occur at the minimum and maximum end of the mass loss range indicating low prediction uncertainty in the prediction. Overall, the results validate the accuracy of the proposed model in estimating mass loss in a consistent and reliable manner.

3.13. Explainability Analysis using SHapley Additive exPlanations (SHAP)

The bar chart in Figure 43 depicts the relative importance of three different features, Gr, SiC, and Al6061, according to their mean absolute SHAP values, which measure the contribution of each feature to the predictions of an ML model. Gr stands out as the most significant feature, with an estimated mean SHAP value of around 220, indicating that it has the greatest impact on the model's predictions. SiC is followed closely with a substantial contribution of 200.

The Al6061 exhibits a lower influence among the three, with a mean SHAP value of approximately 111, which is roughly half as influential as Gr in this particular predictive scenario. Overall, the visualization shows a clear hierarchy of feature importance, with carbon-based and ceramic reinforcements being more important for the model performance than the base Al alloy.

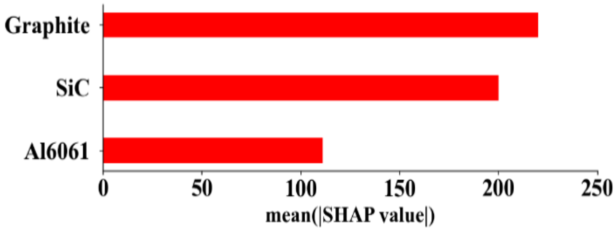

Fig. 43 SHAP Analysis

3.14. K-Fold Cross Validation

The K-fold cross-validation scores for the proposed model and existing ML models over 5 folds are given in Table 10. The proposed model showed the highest accuracy with values ranging from 0.9978 to 0.998 for all folds, which indicates good stability and generalization. The RF model achieved the next best results with scores in the range of 0.962 to 0.964. The SVM model comes next to the RF model, with a score ranging between 0.933 and 0.935.

The MLP model achieved medium performance with a score of approximately 0.916 in Fold 3, and the DT model and the LR model had relatively lower scores. The fold-wise results of the proposed model are minimal, showing that the model is robust and is less sensitive to data partitioning, which confirms that the proposed model is more reliable and effective than the existing approach.

Table 10. K-Fold Cross-Validation Scores of Proposed and Existing Models

Model	Fold 1	Fold 2	Fold 3	Fold 4	Fold 5
Proposed	0.9978	0.998	0.9982	0.9981	0.998
RF	0.9628	0.9635	0.964	0.9632	0.9635
SVM	0.9338	0.9346	0.9352	0.9341	0.9346
MLP	0.9148	0.9153	0.916	0.915	0.9153
DT	0.8905	0.8924	0.8938	0.8912	0.8924
LR	0.8702	0.8716	0.873	0.8698	0.8716

3.15. Ablation Studies

Table 11 presents the ablation analysis of the proposed framework using different model configurations. The baseline DNN model without optimization had the highest prediction errors in all performance measures because of poor convergence capability and inefficient parameter tuning. The MAE, RMSE, and MSE values were significantly decreased, and the R^2 value was significantly increased by introducing the iCSOA optimization algorithm. Using the adaptive depth mechanism in DADNN, the nonlinear feature extraction is further improved, and the generalization performance of the model is further enhanced. The proposed DADNN-iCSOA framework performed best, with the lowest MAE (0.012), RMSE (0.015), MSE (0.0009), MAPE (0.143), and SDE (0.011) values and the highest value for R^2 (0.998). The results show that both adaptive depth learning and optimization using iCSOA make significant contributions to the enhancement of the prediction accuracy and stability.

Table 11. Ablation Analysis of Proposed Model

Model	MAE	RMSE	MSE	R^2	MAPE	SDE
DNN	0.082	0.114	0.0130	0.931	0.624	0.072
DNN + iCSOA	0.041	0.063	0.0040	0.972	0.382	0.041
DADNN	0.028	0.039	0.0015	0.986	0.241	0.026
Proposed DADNN-iCSOA	0.012	0.015	0.0009	0.998	0.143	0.011

3.16. Comparison with Existing Studies

The suggested model demonstrated good accuracy with low error as compared to previous research, suggesting that it can accurately predict the characteristics of Al6061 hybrid composites. The comparison between the suggested model and the existing models is shown in Table 12.

The studies presented in Table 12 focused on the prediction of the composite properties using models such as Deep Long Short-Term Memory (DLSTM), LR model, Sequential Average Generative Discrimination Neural Network (SAGDNN), Hybrid deep neural network-Deer hunting optimization (DNN-DHO), and the proposed model. In contrast to the proposed model, the existing models, such as DLSTM, LR, SAGDNN, and DNN-DHO, often suffer from limited nonlinear learning capability, sensitivity to hyperparameter tuning, poor convergence rate, and reduced generalization performance. The proposed DADNN-iCSOA framework addresses these limitations through adaptive depth learning and optimization-assisted parameter tuning, thus outperforming all the other approaches.

Table 12. Comparative Analysis of the proposed model with Existing Models

Author	Reinforcement Material	Used Technique	Key Findings
Proposed Method	SiC-Gr composites	DADNN-iCSOA	The proposed model achieved 0.012 MAE, 0.015 RMSE, 0.0009 MSE, 0.998 R^2, 0.143 MAPE, and 0.011 SDE, and it exhibited better performance than other models.

Shivashankar et al. [31]	Graphite (Gr) and Tungsten carbide (WC)	Deep Long Short-Term Memory (DLSTM)	For predicting UTS, this model achieved 0.60 RMSE and 0.47 MSE, whereas for predicting hardness, it achieved above 0.37 RMSE and MAE.
Votarikari et al. [32]	Nano-SiO_2	LR model	This model attained 0.95 R^2
Kumar et al. [22]	No Experimental Test	Sequential Average Generative Discrimination Neural Network (SAGDNN)	It achieved an R^2 value of 0.96 in predicting hardness and tensile strength.
Chandrashekhar et al. [33]	Granite particles	Hybrid deep neural network - Deer hunting optimization (DNN-DHO)	This model attained 0.024 RMSE for forecasting mechanical properties

4. Conclusion and Future Work

Al6061-SiC, Al6061-Gr, and Al6061-SiC-Gr hybrid composites were effectively created in this work using two-stage stir casting, and these composites' properties, such as mechanical, tribological, and physical characteristics, were experimentally assessed.

An iCSOA-optimized data-driven DADNN model was created to predict several output qualities at once. The efficacy of the created framework is confirmed by the high degree of agreement between the experimental and anticipated findings.

- The composite of 82 wt.% Al6061, 15 wt.% SiC, and 3 wt.% Gr had better mechanical performance with a maximum UTS of 215 MPa and YS of 165 MPa. The hardness was greatly enhanced, and the highest VHN (102) and BHN (105) were achieved at 15% SiC reinforcement.
- The minimum wear rate was 0.9 mm 3 /N-M, and the minimum mass loss was 4.9 mg in hybrid alloys with high SiC and Gr. The findings of this study show that the composite hard ceramic SiC and lubricating graphite are more effective in improving the wear resistance and durability.
- The developed DADNN-iCSOA was found to be better in predicting the values with an R^2 of about 0.998, an RMSE of about 0.015, and an MSE of about 0.0009. The comparative analysis showed the proposed model is better than existing models such as RF, SVR, DT, LR, and MLP in predicting the composite properties accurately.

Thus, the proposed method reduced the need for extensive experimental tests and enabled an effective design to accurately assess the composite properties. However, the model is limited by a very small dataset. Therefore, the suggested approach may be extended to multi-objective optimization in future research, and its effectiveness can be verified using larger experimental datasets and real-time industrial applications.

Conflict of Interest

The authors declare that they have no conflict of interest.

Funding Information

No funding is provided for the preparation of the manuscript.

Acknowledgement:

None

References

[1] Amlan Kar, Aditya Sharma, and Sachin Kumar, "A Critical Review on Recent Advancements in Aluminium-Based Metal Matrix Composites," *Crystals*, vol. 14, no. 5, pp. 1-41, 2024. [CrossRef] [Google Scholar] [Publisher Link]

[2] Bharat Singh et al., "A Future Prospects and Current Scenario of Aluminium Metal Matrix Composites Characteristics," *Alexandria Engineering Journal*, vol. 76, pp. 1-17, 2023. [CrossRef] [Google Scholar] [Publisher Link]

[3] Dinesh Chawla et al., "Development and Performance Evaluation of AA6061-Sic-Graphite Hybrid Composites for Lightweight Automotive Structural Applications," *Next Materials*, vol. 9, pp. 1-14, 2025. [CrossRef] [Google Scholar] [Publisher Link]

[4] J. Chandradass, T. Thirugnanasambandham, P. Baskara Sethupathi, "Liquid State Stir Cast Processing and Characteristics Study of AZ91D/Sicp Composites," *Materials Today: Proceedings*, vol. 45, pp. 6507-6511, 2021. [CrossRef] [Google Scholar] [Publisher Link]

[5] R. Chitra et al., "Stir Casting Process Parameters and their Influence on the Production of AA6061/B4C Metal Matrix Composites," *Advances in Processing of Lightweight Metal Alloys and Composites*, pp. 193-215, 2022. [CrossRef] [Google Scholar] [Publisher Link]

[6] Ziyauddin Seikh et al., "Metal Matrix Composites Processed through Powder Metallurgy: A Brief Overview," *Journal of the Institution of Engineers (India): Series D*, vol. 106, no. 1, pp. 771-778, 2025. [CrossRef] [Google Scholar] [Publisher Link]

[7] Muhammad Maqbool et al., "3D Interconnected Boron Nitride Macrostructures and Derived Composites for Thermal Energy Regulation," *Advanced Functional Materials*, vol. 35, no. 9, 2025. [CrossRef] [Google Scholar] [Publisher Link]

[8] R.K. Singh, and R.C. Singh, "Property Investigation of Functionally Graded Materials Leaf Spring Plate Fabricated through Stir Casting Process by Using New Gradient Evaluation Method," *Materials Science and Engineering Technology*, vol. 55, no. 9, pp. 1297-309, 2024. [CrossRef] [Google Scholar] [Publisher Link]

[9] Dinesh Kumar, and Lalit Thakur, "Investigation on Mechanical and Wear Performance of Ultrasonic-Assisted Stir Cast AZ91D/Al_2O_3 Magnesium Matrix Composites," *Metals and Materials International*, vol. 29, no. 9, pp. 2767-2781, 2023. [CrossRef] [Google Scholar] [Publisher Link]

[10] Shyam Rangrej et al., "Effects of Stir Casting Process Parameters on Dispersion of Reinforcement Particles during Preparation of Metal Composites," *Materials Today: Proceedings*, vol. 43, pp. 471-475, 2021. [CrossRef] [Google Scholar] [Publisher Link]

[11] Dinesh Chawla, Manoj Nayak, and Pallav Gupta, "Investigating the Effect of Particle Sizes of SiC and Graphite on Strengthening of Aluminium Metal Matrix Composites," *ECS Journal of Solid State Science and Technology*, vol. 13, no. 2, 2024. [CrossRef] [Google Scholar] [Publisher Link]

[12] Prateek Mittal et al., "Characterization of Cu-Graphene Composites Synthesized Through Pressure-Less Sintering for Application in Electrical Contacts," *International Journal on Interactive Design and Manufacturing*, vol. 19, no. 2, pp. 1035-1050, 2025. [CrossRef] [Google Scholar] [Publisher Link]

[13] Prateek Mittal et al., "Synthesis and Characterization of Stir Casted Cu-Zro_2-Graphite Hybrid Metal Matrix Composites for Thermal Management Structures," *Proceedings of the Institution of Mechanical Engineers, Part C: Journal of Mechanical Engineering Science*, vol. 236, no. 14, pp. 7927-7941, 2022. [CrossRef] [Google Scholar] [Publisher Link]

[14] Hoda ElMaraghy, and Waguih ElMaraghy, "Adaptive Cognitive Manufacturing System (ACMS)–A New Paradigm," *International Journal of Production Research*, vol. 60, no. 24, pp. 7436-7449, 2022. [CrossRef] [Google Scholar] [Publisher Link]

[15] Wuxin Sha et al., "Artificial Intelligence to Power the Future of Materials Science and Engineering," *Advanced Intelligent Systems*, vol. 2, no. 4, pp. 1-12, 2020. [CrossRef] [Google Scholar] [Publisher Link]

[16] L. Bharath et al., "Investigative Study on Hardness and Yield Strength of Al6061/Sic/Gr. Hybrid Composite and Prediction using Machine Learning Technique," *Next Research*, vol. 2, no. 3, 2025. [CrossRef] [Google Scholar] [Publisher Link]

[17] Rutuj Rajput, Abhishek Raut, and Srinivasu Gangi Setti, "Prediction of Mechanical Properties of Aluminium Metal Matrix Hybrid Composites Synthesized Using Stir Casting Process by Machine Learning," *Materials Today: Proceedings*, vol. 59, pp. 1735-1742, 2022. [CrossRef] [Google Scholar] [Publisher Link]

[18] M. Nithya et al., "Machine Learning Assisted Investigation on Properties of TiO_2 Reinforced Aluminium Metal Matrix Composites," *Materials Today: Proceedings*, vol. 74, pp. 80-84, 2023. [CrossRef] [Google Scholar] [Publisher Link]

[19] Chitti Babu Golla et al., "Development of Hybrid Aluminum Nanocomposites for Automotive Applications: An In-Depth Analysis Using Experimental Approaches and Predictive Machine Learning Techniques," *Journal of Materials Research and Technology*, vol. 36, pp. 4383-4399, 2025. [CrossRef] [Google Scholar] [Publisher Link]

[20] Mulpur Sarat Babu, Mondi Rama Karthik, and Lakshmi Manasa Birada, "Experimental Study and Machine Learning Modeling of Wear Properties in Al Metal Matrix Composites," *Journal of Tribology*, vol. 148, no. 1, 2026. [CrossRef] [Google Scholar] [Publisher Link]

[21] Mihail Kolev, "A Novel Approach to Predict the Effect of Chemical Composition and Thermo-Mechanical Processing Parameters on Cu–Ni–Si Alloys using a Hybrid Deep Learning and Ensemble Learning Model," *Composites Communications*, vol. 48, pp. 1-2024. [CrossRef] [Google Scholar] [Publisher Link]

[22] P. Saravana Kumar et al., "Identification and Optimization of Mechanical Characteristics in Graphene-Reinforced Aluminum Matrix Composites based on Artificial Intelligence," *Composites Part B: Engineering*, vol. 311, 2026. [CrossRef] [Google Scholar] [Publisher Link]

[23] Namrata Mishra, and Annasamy Baradeswaran, "High-Temperature Tribology of AA7075-Tib_2/Aln Composites: Experiments, Response-Surface Optimisation, and Interpretable Machine Learning," *Multiscale and Multidisciplinary Modeling, Experiments and Design*, vol. 9, no. 1, pp. 1-15, 2026. [CrossRef] [Google Scholar] [Publisher Link]

[24] Selvarasu Saminathan, and Jayakumar Lakshmipathy, "Experimental Investigation and Prediction Analysis on Granite/SiC Reinforced Al7050 and Al7075 Using Hybrid Deep Neural Network Based Salp Swarm Optimization," *Silicon*, vol. 14, no. 11, pp. 5887-5903, 2022. [CrossRef] [Google Scholar] [Publisher Link]

[25] Halil Karakoç et al., "Wear and Mechanical Properties of Al6061/Sic/B4C Hybrid Composites Produced with Powder Metallurgy," *Journal of Materials Research and Technology*, vol. 8, no. 6, pp. 5348-5361, 2019. [CrossRef] [Google Scholar] [Publisher Link]

[26] P. Bharathi, and T. Sampath Kumar, "Effect of Silicon Carbide and Boron Carbide on Mechanical and Tribological Properties of Aluminium 7075 Composites for Automobile Applications," *Silicon*, vol. 15, no. 14, pp. 6147-6171, 2023. [CrossRef] [Google Scholar] [Publisher Link]

[27] Pooja Verma et al., "Mechanical and Wear Properties of Graphite Reinforced Aluminum Metal Matrix Composites Processed by Ultrasonic-Stir-Squeeze Casting," *Journal of Materials Engineering and Performance*, vol. 33, no. 11, pp. 5319-5330, 2024. [CrossRef] [Google Scholar] [Publisher Link]

[28] J. Chandradass et al., “Effect of Silicon Carbide and Silicon Carbide/Alumina Reinforced Aluminum Alloy (AA6061) Metal Matrix Composite,” *Materials Today: Proceedings*, vol. 45, pp. 7147-7150, 2021. [CrossRef] [Google Scholar] [Publisher Link]

[29] Davies Oladayo Folorunso, and Seun Samuel Owoeye, “Influence of Quarry Dust-Silicon Carbide Weight Percentage on the Mechanical Properties and Tribological Behavior of Stir Cast ZA-27 Alloy Based Hybrid Composites,” *Journal of King Saud University-Engineering Sciences*, vol. 31, no. 3, pp. 280-285, 2019. [CrossRef] [Google Scholar] [Publisher Link]

[30] D. Mohana Krishnudu et al., “Effect of Fiber Content and Wear Parameters on Abrasive Wear Behaviour of Abutilon Indicum Fiber Reinforced Epoxy Composites and Its Prediction Using ANFIS,” *Hybrid Advances*, vol. 3, pp. 1-8, 2023. [CrossRef] [Google Scholar] [Publisher Link]

[31] R. Shivashankar et al., “Development and Mechanical Characterisation of Hybrid Tungsten Carbide/Graphite Reinforced Aluminium Metal Matrix Composites Using Deep Learning Techniques,” *Canadian Metallurgical Quarterly*, vol. 65, no. 1, pp. 334-349, 2026. [CrossRef] [Google Scholar] [Publisher Link]

[32] Naveen Kumar Votarikari, N. Kishore Nath, and P. Ramesh Babu, “Evaluating and Optimising Tribological Parameters of Enhanced Two-Step Stir Cast Al6061/Nano-SiO_2 Composite Using Machine Learning Techniques,” *Journal of Bio-and Tribo-Corrosion*, vol. 10, no. 3, 2024. [CrossRef] [Google Scholar] [Publisher Link]

[33] Koli Gajanan Chandrashekhar, D.P. Girish, and Katkar Ajit Ashok, “Optimization and Prediction on the Mechanical Behavior of Granite Particle Reinforced Al6061 Matrix Composites Using Deer Hunting Optimization Based DNN,” *Silicon*, vol. 14, no. 14, pp. 8745-8763, 2022. [CrossRef] [Google Scholar] [Publisher Link]